Marine terraces of the last interglacial period along the Pacific coast of South America (1°N-40°S)

Roland Freisleben[1], Julius Jara-Muñoz[1], Daniel Melnick[2,3], José Miguel Martínez[2,3], Manfred R. Strecker[1]

[1] Institut für Geowissenschaften, Universität Potsdam, 14476 Potsdam, Germany
[2] Instituto de Ciencias de la Tierra, TAQUACH, Universidad Austral de Chile, Valdivia, Chile
[3] Millennium Nucleus The Seismic Cycle Along Subduction Zones, Valdivia, Chile

Correspondence to: Roland Freisleben (freisleb@uni-potsdam.de)

Abstract. Tectonically active coasts are dynamic environments characterized by the presence of multiple marine terraces formed by the combined effects of wave-erosion, tectonic uplift, and sea-level oscillations at glacial-cycle timescales. Well-preserved erosional terraces from the last interglacial sea-level highstand are ideal marker horizons for reconstructing past sea-level positions and calculating vertical displacement rates. We carried out an almost continuous mapping of the last interglacial marine terrace along ~5,000 km of the western coast of South America between 1°N and 40°S. We used quantitatively replicable approaches constrained by published terrace-age estimates to ultimately compare elevations and patterns of uplifted terraces with tectonic and climatic parameters in order to evaluate the controlling mechanisms for the formation and preservation of marine terraces, and crustal deformation. Uncertainties were estimated on the basis of measurement errors and the distance from referencing points. Overall, our results indicate a median elevation of 30.1 m, which would imply a median uplift rate of 0.22 m/ka averaged over the past ~125 ka. The patterns of terrace elevation and uplift rate display high-amplitude (~100–200 m) and long-wavelength (~10^2 km) structures at the Manta Peninsula (Ecuador), the San Juan de Marcona area (central Peru), and the Arauco Peninsula (south-central Chile). Medium-wavelength structures occur at the Mejillones Peninsula and Topocalma in Chile, while short-wavelength (< 10 km) features are for instance located near Los Vilos, Valparaíso, and Carranza, Chile. We interpret the long-wavelength deformation to be controlled by deep-seated processes at the plate interface such as the subduction of major bathymetric anomalies like the Nazca and Carnegie ridges. In contrast, short-wavelength deformation may be primarily controlled by sources in the upper plate such as crustal faulting, which, however, may also be associated with the subduction of topographically less pronounced bathymetric anomalies. Latitudinal differences in climate additionally control the formation and preservation of marine terraces. Based on our synopsis we propose that increasing wave height and tidal range result in enhanced erosion and morphologically well-defined marine terraces in south-central Chile. Our study emphasizes the importance of using systematic measurements and uniform, quantitative methodologies to characterize and correctly interpret marine terraces at regional scales, especially if they are used to unravel tectonic and climatic forcing mechanisms of their formation. This database is an integral part of the World Atlas of Last Interglacial Shorelines (WALIS), published online at http://doi.org/10.5281/zenodo.4309748 (Freisleben et al., 2020).

1. Introduction

Tectonically active coasts are highly dynamic geomorphic environments and they host densely-populated centers and associated infrastructure (Melet et al., 2020). Coastal areas have been episodically affected by the effects of sea-level changes at glacial timescales, modifying the landscape and leaving behind fossil geomorphic markers, such as former paleo-shorelines, and marine terraces (Lajoie, 1986). One of the most prominent coastal landforms are marine terraces that were generated during the protracted last interglacial sea-level highstand that occurred ~125 ka ago (Siddall et al., 2006; Hearty et al., 2007; Pedoja et al., 2011). These terraces are characterized by a higher preservation potential, which facilitates their recognition, mapping, and lateral correlation. Furthermore, because of their high degree of preservation and relatively young age, they have been used to estimate vertical deformation rates at local and regional scales. The relative abundance and geomorphic characteristics of the last interglacial marine terraces make them ideal geomorphic markers with which to reconstruct past sea-level positions and to enable comparisons between distant sites under different climatic and tectonic settings.

The Western South American Coast (WSAC) is a tectonically active region that has been repeatedly affected by megathrust earthquakes and associated surface deformation (Beck et al., 1998; Melnick et al., 2006; Bilek, 2010; Baker et al., 2013). Interestingly, previous studies have shown that despite the broad spectrum of latitudinal climatic conditions and erosional regimes along the WSAC, marine terraces are scattered, but omnipresent along the coast (Ota et al., 1995; Regard et al., 2010; Rehak et al., 2010; Bernhardt et al., 2016; Melnick, 2016; Bernhardt et al., 2017). However, only a few studies on interglacial marine terraces have been conducted along the WSAC, primarily in specific areas where they are best expressed; this has resulted in disparate and inconclusive marine terrace measurements based on different methodological approaches and ambiguous interpretations concerning their origin in a tectonic and climatic context (Hsu et al., 1989; Ortlieb and Macharé, 1990; Hsu, 1992; Macharé and Ortlieb, 1992; Pedoja et al., 2006b; Saillard et al., 2009; Pedoja et al., 2011; Saillard et al., 2011; Rodríguez et al., 2013). This lack of reliable data points has revealed a need to re-examine the last interglacial marine terraces along the WSAC based on standardized methodologies in order to obtain a systematic and continuous record of marine terrace elevations along the coast. This information is crucial in order to increase our knowledge of the climatic and tectonic forcing mechanisms that contributed to the formation and degradation of marine terraces in this region.

Marine terrace sequences at tectonically active coasts are landforms formed by wave erosion and/or accumulation of sediments resulting from the interaction between tectonic uplift and superposed oscillating sea-level changes (Lajoie, 1986; Anderson et al., 1999; Jara-Muñoz et al., 2015). Typically, marine terrace elevations are estimated based on the shoreline angle. The marine terrace morphology comprises a gently inclined erosional or depositional paleo-platform that terminates landward at a steeply sloping paleo-cliff surface. The intersection point between both surfaces represents the approximate sea-level position during the formation of the marine terrace also known as shoreline angle; if coastal uplift is rapid, such uplifting abrasion or depositional surfaces may be preserved in the landscape and remain unaltered by the effects of subsequent sea-level oscillations (Lajoie, 1986).

68 The analysis of elevation patterns based on shoreline-angle measurements at subduction margins has been largely used

69 to estimate vertical deformation rates and the mechanisms controlling deformation, including the interaction of the

70 upper plate with bathymetric anomalies, the activity of crustal faults in the upper plate, and deep-seated processes

71 such as basal accretion of subducted trench sediments (Taylor et al., 1987; Hsu, 1992; Macharé and Ortlieb, 1992; Ota

72 et al., 1995; Pedoja et al., 2011; Saillard et al., 2011; Jara-Muñoz et al., 2015; Melnick, 2016). The shoreline angle

73 represents a 1D descriptor of the marine terrace elevation, whose measurements are reproducible when using

74 quantitative morphometric approaches (Jara-Muñoz et al., 2016). Furthermore, the estimation of the marine terrace

75 elevations based on shoreline angles can be further improved by quantifying their relationship with paleo-sea level,

76 also known as the indicative meaning (Lorscheid and Rovere, 2019).

77 In this continental-scale compilation of marine terrace elevations along the WSAC, we present systematically mapped

78 shoreline angles of marine terraces of the last (Eem/Sangamon) interglacial obtained along 5,000 km of coastline

79 between 1°N and 40°S. In this synthesis we rely on chronological constraints from previous regional studies and

80 compilations (Pedoja et al., 2011). For the first time we are able to introduce an almost continuous pattern of terrace

81 elevation and coastal uplift rates at a spatial scale of 10^3 km along the WSAC. Furthermore, in our database we

82 compare tectonic and climatic parameters to elucidate the mechanisms controlling the formation and preservation of

83 marine terraces, and patterns of crustal deformation along the coast. This study was thus primarily intended to provide

84 a comprehensive, standardized database and description of last interglacial marine terrace elevations along the

85 tectonically active coast of South America. This database therefore affords future research into coastal environments

86 to decipher potential tectonic forcings with regard to the deformation and seismotectonic segmentation of the forearc;

87 as such this database will ultimately help to decipher the relationship between upper-plate deformation, vertical motion

88 and bathymetric anomalies and aid in the identification of regional fault motions along pre-existing anisotropies in the

89 South American continental plate. Finally, our database includes information on climate-driving forcing mechanisms

90 that may influence the formation, modification and/or destruction of marine terraces in different climatic sectors along

91 the South American convergent margin. This new database is part of the World Atlas of Last Interglacial Shorelines

92 (WALIS), published online at http://doi.org/10.5281/zenodo.4309748 (Freisleben et al., 2020).

93 **2. Geologic and geomorphic setting of the WSAC**

94 **2.1. Tectonic and seismotectonic setting**

95 **2.1.1. Subduction geometry and bathymetric features**

96 The tectonic setting of the convergent margin of South America is controlled by subduction of the oceanic Nazca plate

97 beneath the South American continental plate. The convergence rate varies between 66 mm/a in the north (8°S latitude)

98 and 74 mm/a in the south (27°S latitude) (Fig. 1). The convergence azimuth changes slightly from N81.7° toward

99 N77.5° from north to south (DeMets et al., 2010). The South American subduction zone is divided into four major

100 segments with variable subduction angles inferred from the spatial distribution of Benioff seismicity (Barazangi and

101 Isacks, 1976; Jordan et al., 1983) (Fig. 1). The segments beneath northern and central Peru (2°–15°S) and beneath

102   central Chile (27°–33°S) are characterized by a gentle dip of the subducting plate between 5° and 10° at depths of

103   ~100 km (Hayes et al., 2018), whereas the segments beneath southern Peru and northern Chile (15°–27°S), and beneath

104   southern Chile (33°–45°S) have steeper dips of 25° to 30°. Spatial distributions of earthquakes furthermore indicate a

105   steep-slab subduction segment in Ecuador and southern Colombia (2°S to 5°N), and a flat-slab segment in NW

106   Colombia (north of 5°N) (Pilger, 1981; Cahill and Isacks, 1992; Gutscher et al., 2000; Ramos and Folguera, 2009).

107   Processes that have been inferred to be responsible for the shallowing of the subduction slab include the subduction

108   of large buoyant ridges or plateaus (Espurt et al., 2008) as well as the combination of trenchward motion of thick,

109   buoyant continental lithosphere accompanied by trench retreat (Sobolev and Babeyko, 2005; Manea et al., 2012).

110   Volcanic activity as well as the forearc architecture and distribution of upper-plate deformation further emphasize the

111   location of flat-slab subduction segments (Jordan et al., 1983; Kay et al., 1987; Ramos and Folguera, 2009).

112   Several high bathymetric features have been recognized on the subducting Nazca plate. The two most prominent

113   bathymetric features being subducted beneath South America are the Carnegie and Nazca aseismic ridges at 0° and

114   15°S, respectively; they consist of seamounts related to hot-spot volcanism (Gutscher et al., 1999; Hampel, 2002).

115   The 300-km-wide and ~2-km-high Carnegie Ridge subducts roughly parallel with the convergence direction and its

116   geometry should have remained relatively stable beneath the continental plate (Angermann et al., 1999; Gutscher et

117   al., 1999; DeMets et al., 2010; Martinod et al., 2016a). In contrast, the obliquity of the 200-km-wide and 1.5-km-high

118   Nazca Ridge with respect to the convergence direction resulted in 500 km SE-directed migration of its locus of ridge

119   subduction during the last 10 Ma (Hampel, 2002; Saillard et al., 2011; Martinod et al., 2016a). Similarly, smaller

120   aseismic ridges such as the Juan Fernández Ridge and the Iquique Ridge subduct beneath the South American

121   continent at 32°S and 21°S, respectively. The intercepts between these bathymetric anomalies and the upper plate are

122   thought to influence the characteristics of interplate coupling and seismic rupture (Bilek et al., 2003; Wang and Bilek,

123   2011; Geersen et al., 2015; Collot et al., 2017) and mark the boundaries between flat and steep subduction segments

124   and changes between subduction erosion and accretion (Jordan et al., 1983; von Huene et al., 1997; Ramos and

125   Folguera, 2009) (Fig. 1).

126   In addition to bathymetric anomalies, several studies have shown that variations in the volume of sediments in the

127   trench may control the subduction regime from an erosional mode to an accretionary mode (von Huene and Scholl,

128   1991; Bangs and Cande, 1997). In addition, the volume of sediment in the trench has also been hypothesized to

129   influence the style of interplate seismicity (Lamb and Davis, 2003). At the southern Chile margin, thick trench-

130   sediment sequences and a steeper subduction angle correlate primarily with subduction accretion, although the area

131   of the intercept of the continental plate with the Chile Rise spreading center locally exhibits the opposite case (von

132   Huene and Scholl, 1991; Bangs and Cande, 1997). Subduction erosion characterizes the region north of the southern

133   volcanic zone from central and northern Chile to southern Peru (33°–15°S) due to decreasing sediment supply to the

134   trench, especially within the flat-slab subduction segments (Stern, 1991; von Huene and Scholl, 1991; Bangs and

135   Cande, 1997; Clift and Vannucchi, 2004). Clift and Hartley (2007) and Lohrmann et al. (2003) argued for an alternate

136   style of slow tectonic erosion leading to underplating of subducted material below the base of the crustal forearc,

137   synchronous with tectonic erosion beneath the trenchward part of the forearc. For the northern Andes, several authors

138   also classify the subduction zone as an erosional type (Clift and Vannucchi, 2004; Scholl and Huene, 2007; Marcaillou

139   et al., 2016).

2.1.2. Major continental fault systems in the coastal realm

141   The South American convergent margin comprises several fault systems with different kinematics, whose presence is

142   closely linked to oblique subduction and the motion and deformation of forearc slivers. Here we summarize the main

143   structures that affect the Pacific coastal areas. North of the Talara bend (5°S), active thrusting and dextral strike-slip

144   faulting dominates the coastal lowlands of Ecuador (e.g., Mache, Bahía, Jipijapa faults), although normal faulting also

145   occurs at Punta Galera (Cumilínche fault) and the Manta Peninsula (Río Salado fault) (Fig. 1). Farther south, normal

146   faulting is active in the Gulf of Guayaquil (Posorja fault) and dextral strike-slip faulting occurs at the Santa Elena

147   Peninsula (La Cruz fault) (Veloza et al., 2012; Costa et al., 2020). The most prominent dextral fault in this region is

148   the 2000-km-long, northeast-striking Dolores-Guayaquil megashear (DGM), which starts in the Gulf of Guayaquil

149   and terminates in the Colombian hinterland east of the range-bounding thrust faults of the Colombian Andes (Veloza

150   et al., 2012; Villegas-Lanza et al., 2016; Costa et al., 2020) (Fig. 1). Normal faults have been described along the coast

151   of Peru at the Illescas Peninsula in the north (6°S), ~~in the San Juan de Marcona area~~ with~~in~~ the El Huevo–Lomas fault

152   system in the San Juan de Marcona area (14.5°–16°S), and within the Incapuquio fault system ~~in the~~farther south

153   (17°–18°S) (Veloza et al., 2012; Villegas-Lanza et al., 2016; Costa et al., 2020). The main fault zones of the Chilean

154   convergent margin comprise the Atacama Fault System (AFS) in the Coastal Cordillera extending from Iquique to La

155   Serena (29.75°S, Fig. 1), with predominantly N-S-striking normal faults, which result in relative uplift of their western

156   side (e.g., Mejillones fault, Salar del Carmen fault) (Naranjo, 1987; González and Carrizo, 2003; Cembrano et al.,

157   2007). Coastal fault systems farther south are located in the Altos de Talinay area (30.5°S, Puerto Aldea fault), near

158   Valparaíso (33°S, Quintay and Valparaíso faults), near the Arauco Peninsula (36°–39°S, Santa María and Lanalhue

159   faults), and in between these areas (Topocalma, Pichilemu, Carranza, and Pelluhue faults) (Ota et al., 1995; Melnick

160   et al., 2009; Santibáñez et al., 2019; Melnick et al., 2020; Maldonado et al., 2021) (Fig. 1). However, there is still

161   limited knowledge regarding Quaternary slip rates and kinematics and, most importantly, the location of active faults

162   along the forearc region of South America (Jara-Muñoz et al., 2018; Melnick et al., 2019).

2.2. Climate and geomorphic setting

2.2.1. Geomorphology

165   The 8000-km-long Andean orogen is a major, hemisphere-scale feature that can be divided into ~~different~~ segments

166   with distinctive geomorphic and tectonic characteristics. The principal segments comprise the NNE-SSW trending

167   Colombian-Ecuadorian segment (12°N–5°S), the NW-SE oriented Peruvian segment (5°–18°S), and the N-S trending

168   Chilean segment (18°–56°S) (Jaillard et al., 2000) (Fig. 1). Two major breaks separate these segments; these are the

169   Huancabamba bend in northern Peru and the Arica bend at the Peru-Chile border. The distance of the trench from the

170   WSAC coastline averages 118 km and ranges between 44 and 217 km. The depth of the trench ~~fluctuates~~ varies

171   between

Figure 1. (A) Morphotectonic setting of the South American margin showing major fault systems/crustal faults (Costa et al., 2000; Veloza et al., 2012; Melnick et al., 2020), slab depth (Hayes et al., 2018), and flat-slab subduction segments, active volcanos (Venzke, 2013), bathymetric features of the subducting plate, trench-sediment thickness (Bangs and Cande, 1997), segments of subduction erosion and accretion (Clift and Vannucchi, 2004), plate age (Müller et al., 2008), convergence vectors (DeMets et al., 2010), and marine terrace ages used for lateral correlation. DGM: Dolores-Guayaquil megashear, AFS: Atacama Fault System, LOFZ: Liquiñe-Ofqui Fault Zone, FZ: Fracture Zone, 1: Punta Galera, 2: Manta Pen., 3: Gulf of Guayaquil / Santa Elena Pen., 4: Tablazo Lobitos, 5: Paita Pen., 6: Illescas Pen., 7: Chiclayo, 8: Lima, 9: San Juan de Marcona, 10: Chala Bay, 11: Pampa del Palo, 12: Pisagua, 13: Iquique, 14: Tocopilla, 15: Mejillones Pen., 16: Taltal, 17: Caldera, 18: Punta Choros, 19: Altos de Talinay, 20: Los Vilos, 21: Valparaíso, 22: Topocalma, 23: Carranza, 24: Arauco Pen., 25: Valdivia (World Ocean Basemap: Esri, Garmin, GEBCO, NOAA NGDC, and other contributors). **(B)** Location of the study area.

173 2920 and 8177 m (GEBCO Bathymetric Compilation Group, 2020), and the continental shelf has an average width of
174 28 km (Paris et al., 2016).

175 In the 50- to 180-km-wide coastal area of the Ecuadorian Andes, where the Western Cordillera is flanked by a
176 structural depression, relief is relatively low (< 300 m asl). The Gulf of Guayaquil (3°S) and the Dolores-Guayaquil
177 megashear separate the northern from the southern forearc units. The coast-trench distance along the Huancabamba
178 bend is quite small (~55–90 km), except for the Gulf of Guayaquil, and the trench east of the Carnegie Ridge is at a
179 relatively shallow depth of ~3.5 km. Farther south, the Peruvian forearc comprises the up to 160-km-wide Coastal
180 Plains in the north and the narrow, 3000-m-high Western Cordillera. While the Coastal pPlains in north-central Peru
181 are relatively narrow (< 40 km), they widen in southern Peru, and the elevation of the Western Cordillera increases to
182 more than 5000 m (Suárez et al., 1983; Jaillard et al., 2000). The region between the coast and the trench in central
183 Peru (up to 220 km) narrows toward the San Juan de Marcona area (~75 km) near the intercept with the Nazca Ridge,
184 and the relatively deep trench (~6.5 km) becomes shallower (< 5 km) (GEBCO Bathymetric Compilation Group,
185 2020). Between 18°S and 28°S, the Chilean forearc comprises the 50-km-wide and up to 2700-m-high Coastal
186 Cordillera, which is separated from the Precordillera by the Central Depression. In the flat-slab subduction segment
187 between 27°S and 33°S there is neither a morphotectonic region characterized by a central depression nor active
188 volcanism in the high Andean cordillera (Fig. 1) (Jordan et al., 1983). The Chilean forearc comprises the Coastal
189 Cordillera, which varies in altitude from up to 2000 m at 33°S to 500 m at 46°S, and the Central Depression that
190 separates the forearc from the Main Cordillera. From the Arica bend, where the coast-trench distance is up to 170 km
191 and the trench ~8 km deep, a slight increase in coast-trench distance can be observed in Chile toward the south (~80–
192 130 km), as can a decrease in trench depth to ~4.5 km.

2.2.2. Marine terraces and coastal uplift rates

194 Wave erosion forms generates wave-cut terrace levels, while the accumulation of shallow marine sediments during
195 sea-level highstands forms wave-built terraces. Another type of terrace is known as "rasa" and refers to wide shore
196 platforms formed under slow-uplift conditions (< 0.2 m/ka), and the repeated reoccupation of this surface by high sea
197 levels (Regard et al., 2010; Rodríguez et al., 2013; Melnick, 2016). Other studies indicate a stronger influence of
198 climate and rock resistance to erosion compared to marine wave action (Prémaillon et al., 2018). Typically, the
199 formation of Pleistocene marine terraces in the study area occurred during interglacial and interstadial relative sea-
200 level highstands that were superposed on the uplifting coastal areas; according to the Quaternary oxygen-isotope curve
201 defining warm and cold periods, high Quaternary sea levels have been correlated with warm periods and are denoted
202 with the odd-numbered Marine Isotope Stages (MIS) (Lajoie, 1986; Shackleton et al., 2003).

203 Along the WSAC, staircase-like sequences of multiple marine terraces are preserved nearly continuously along the
204 coast. These terraces comprise primarily wave-cut surfaces that are frequently covered by beach ridges of siliciclastic
205 sediments and local accumulations of carbonate bioclastic materials associated with beach ridges (Ota et al., 1995;
206 Saillard et al., 2009; Rodríguez et al., 2013; Martinod et al., 2016b). Rasa surfaces exist in the regions of southern
207 Peru and northern Chile (Regard et al., 2010; Rodríguez et al., 2013; Melnick, 2016). Particularly the well-preserved

208 MIS-5e terrace level has been largely used as a strain marker in the correlation of uplifted coastal sectors due to its

209 lateral continuity and high potential for preservation. Global observations of sea-level fluctuations during MIS-5 allow

210 to differentiate between three second-order highstands at 80 ka (5a), 105 ka (5c), and 128 to 116 ka (5e) with paleo-

211 sea levels of -20 m for both of the younger and +3 ± 3 m for the oldest highstand (Stirling et al., 1998; Siddall et al.,

212 2006; Hearty et al., 2007; Rohling et al., 2009; Pedoja et al., 2011), although glacio-isostatic adjustments (GIA) can

213 cause local differences of up to 30 m (Simms et al., 2016; Creveling et al., 2017). The database generated in this study

214 is based exclusively in the last interglacial marine terraces exposed along the WSAC, between Ecuador and Southern

215 Chile (1°S to 40°S). In the following section we present a brief review of previously studied marine terrace sites in

216 this area.

217 Paleo-shoreline elevations of the last interglacial (MIS-5e) in Ecuador are found at elevations of around 45 ± 2 m asl

218 in Punta Galera (Esmeraldas area), 43–57 ± 2 m on the Manta Peninsula and La Plata Island, and 15 ± 5 m asl on the

219 Santa Elena Peninsula (Pedoja et al., 2006b; Pedoja et al., 2006a). In northern Peru, MIS-5e terraces have been

220 described at elevations of 18–31 m asl for the Tablazo Lobitos (Cancas and Mancora areas), at 25 ± 5 m asl on the

221 Paita Peninsula, and at 18 ± 3 m asl on the Illescas Peninsula and the Bay of Bayovar (Pedoja et al., 2006b). Farther

222 south, MIS-5e terraces are exceptionally high in the San Juan de Marcona area immediately south of the subducting

223 Nazca Ridge, with maximum elevations of 80 m at the Cerro Tres Hermanas and 105 m at the Cerro El Huevo (Hsu

224 et al., 1989; Ortlieb and Macharé, 1990; Saillard et al., 2011). The Pampa del Palo region in southern Peru exhibits

225 relatively thick vertical stacks of shallow marine terrace deposits related to MIS-7, 5e (~20 m), and 5c that may

226 indicate a different geodynamic behavior compared to adjacent regions (Ortlieb et al., 1996b). In central and northern

227 Chile, the terrace levels of the last interglacial occur at 250–400 m, 150–240 m, 80–130 m, and 30–40 m, and in

228 southern Chile at 170–200 m, 70 m, 20–38 m, 8–10 m (Fuenzalida et al., 1965). Specifically, between 24°S and 32°S,

229 paleo-shoreline elevations of the last interglacial (MIS-5e) range between 25 and 45 m (Ota et al., 1995; Saillard et

230 al., 2009; Martinod et al., 2016b). Shore platforms are higher in the Altos de Talinay area (30.3°–31.3°S), but are

231 small, poorly preserved, and terminate at a high coastal scarp between 26.75°S and 24°S (Martinod et al., 2016b).

232 Shoreline-angle elevations between 34° and 38°S (along the Maule seismotectonic segment) vary from high altitudes

233 in the Arauco and Topocalma areas (200 m) to moderate elevations near Caranza (110 m), and very low elevations in

234 between (15 m) (Melnick et al., 2009; Jara-Muñoz et al., 2015).

235 Coastal uplift-rate estimates along the WSAC mainly comprise calculations for the Talara Arc, the San Juan de

236 Marcona area, the Mejillones Peninsula, the Altos de Talinay area, and several regions in south-central Chile. Along

237 the Talara Arc (6.5°S to 1°N), marine terraces of the Manta Peninsula and La Plata Island in central Ecuador indicate

238 the most pronounced uplift rates of 0.31 to 0.42 m/ka since MIS-5e, while similar uplift rates are documented to the

239 north in the Esmeraldas area (0.34 m/ka), and lower ones to the south at the Santa Elena Peninsula (0.1 m/ka). In

240 northern Peru, last interglacial uplift rates are relative low, ranging from 0.17–0.21 m/ka for the Tablazo Lobitos and

241 0.16 m/ka for the Paita Peninsula, to 0.12 m/ka for the Bay of Bayovar and the Illescas Peninsula (Pedoja et al., 2006b;

242 Pedoja et al., 2006a). Marine terraces on the continental plate above the subducting Nazca Ridge (13.5°–15.6°S) record

243 variations in uplift rate where the coastal forearc above the northern flank of the ridge is either stable or has undergone

244 net subsidence (Macharé and Ortlieb, 1992). The coast above the ridge crest is rising at about 0.3 m/ka and the coast

245 above the southern flank (San Juan de Marcona) is uplifting at a rate of 0.5 m/ka (Hsu, 1992) or even 0.7 m/ka (Ortlieb

246 and Macharé, 1990) for at least the last 125 ka. Saillard et al. (2011) state that long-term regional uplift in the San

247 Juan de Marcona area has increased since about 800 ka related to the southward migration of the Nazca Ridge, and

248 ranges from 0.44 to 0.87 m/ka. The Pampa del Palo area in southern Peru rose more slowly or was even down-faulted

249 and had subsided with respect to the adjacent coastal regions (Ortlieb et al., 1996b). These movements ceased after

250 the highstand during the MIS-5e and slow uplift rates of approximately 0.16 m/ka have characterized the region since

251 100 ka (Ortlieb et al., 1996b). In northern Chile (24°–32°S), uplift rates for the Late Pleistocene average around 0.28

252 $\pm$ 0.15 m/ka (Martinod et al., 2016b), except for the Altos de Talinay area, where pulses of rapid uplift occurred during

253 the Middle Pleistocene (Ota et al., 1995; Saillard et al., 2009; Martinod et al., 2016b). The Central Andean rasa (15°–

254 33°S) and Lower to Middle Pleistocene shore platforms – which are also generally wider – indicate a period of tectonic

255 stability or subsidence followed by accelerated and spatially continuous uplift after ~400 ka (MIS-11) (Regard et al.,

256 2010; Rodríguez et al., 2013; Martinod et al., 2016b). However, according to Melnick (2016), the Central Andean rasa

257 has experienced slow and steady long-term uplift with a rate of 0.13 ± 0.04 m/ka during the Quaternary, predominantly

258 accumulating strain through deep earthquakes at the crust-mantle boundary (Moho) below the locked portion of the

259 plate interface. The lowest uplift rates occur at the Arica bend and increase gradually southward; the highest values

260 are attained along geomorphically distinct peninsulas (Melnick, 2016). In the Maule segment (34°-38°S), the mean

261 uplift rate for the MIS-5 terrace level is 0.5 m/ka, exceeded only in the areas of Topocalma, Carranza, and Arauco,

262 where it amounts to 1.6 m/ka (Melnick et al., 2009; Jara-Muñoz et al., 2015). Although there are several studies of

263 marine terraces along the WSAC, these are isolated and based on different methodological approaches, mapping and

264 leveling resolution, as well as dating techniques, which makes regional comparisons and correlations difficult in the

265 context of the data presented here.

2.2.3. Climate

267 Apart from latitudinal temperature changes, the present-day morphotectonic provinces along the South American

268 margin have a pronounced impact on the precipitation gradients on the west coast of South America. Since mountain

269 ranges are oriented approximately perpendicular to moisture-bearing winds, they affect both flanks of the orogen

270 (Strecker et al., 2007). The regional-scale pattern of wind circulation is dominated by westerly winds at

271 subtropical/extratropical latitudes primarily up to about 27°S (Garreaud, 2009). However, anticyclones over the South

272 Pacific result in winds blowing from the south along the coast between 35°S and 10°S (Garreaud, 2009). The moisture

273 in the equatorial Andes (Ecuador and Colombia) and in the areas farther south (27°S) is fed by winds from the Amazon

274 basin and the Gulf of Panama, resulting in rainfall mainly on the eastern flanks of the mountain range (Bendix et al.,

275 2006; Bookhagen and Strecker, 2008; Garreaud, 2009). The Andes of southern Ecuador, Peru, and northern Chile are

276 dominated by a rain-shadow effect that causes aridity within the Andean Plateau (Altiplano-Puna), the Western

277 Cordillera, and the coastal region (Houston and Hartley, 2003; Strecker et al., 2007; Garreaud, 2009). Furthermore,

278 the aridity is exacerbated by the effects of the cold Humboldt current, which prevents humidity from the Pacific from

279 penetrating inland (Houston and Hartley, 2003; Garreaud, 2009; Coudurier-Curveur et al., 2015). The precipitation

280 gradient reverses between 27°S and 35°S, where the Southern Hemisphere Westerlies cause abundant rainfall on the
281 western flanks of the Coastal and Main cordilleras (Garreaud, 2009). Martinod et al. (2016b) proposed that latitudinal
282 differences in climate largely influence coastal morphology, specifically the formation of high coastal scarps that
283 prevent the development of extensive marine terrace sequences. However, the details of this relationship have not
284 been conclusively studied along the full extent of the Pacific coast of South America.

3. Methods

286 We combined – and describe in detail below – bibliographic information, different topographic data sets, and uniform
287 morphometric and statistical approaches to assess the elevation of marine terraces and accompanying vertical
288 deformation rates along the western South American margin.

3.1. Mapping of marine terraces

290 Marine terraces are primarily described based on their elevation, which is essential for determining vertical
291 deformation rates. The measurements of the marine terrace elevations of the last interglacial were performed using
292 TanDEM-X topography (12 and 30 m horizontal resolution) (German Aerospace Center (DLR), 2018), and digital
293 terrain models from LiDAR (1, 2.5, and 5 m horizontal resolution). The DEMs were converted to orthometric heights
294 by subtracting the EGM2008 geoid and projected in UTM using the World Geodetic System (WGS1984) using zone
295 19S for Chile, zone 18S for southern/central Peru, and zone 17S for northern Peru/Ecuador.

296 To trace the MIS-5 shoreline, we mapped its inner edge along the west coast of South America based on slope changes
297 on TanDEM-X topography at the foot of paleo-cliffs (Jara-Muñoz et al., 2016) (Fig. 2A and B). To facilitate mapping,
298 we used slope and hillshade maps. We correlated the results of the inner-edge mapping with the marine terraces catalog
299 of Pedoja et al. (2011) and references therein (section 2.2.2, Table 1). Further references used to validate MIS-5e
300 terrace heights include Victor et al. (2011) for the Pampa de Mejillones, Martinod et al. (2016b) for northern Chile,
301 and Jara-Muñoz et al. (2015) for the area between 34° and 38°S. We define the term "referencing point" for these
302 previously published terrace heights and age constraints. The referencing point with the shortest distance to the
303 location of our measurements served as a topographical and chronological benchmark for mapping the MIS-5 terrace
304 in the respective areas. In addition, this distance is used to assign a quality rating to our measurements.

305 In addition to MIS-5e, we also mapped MIS-5c in areas with high uplift rates such as at the Manta Peninsula, San
306 Juan de Marcona, Topocalma, Carranza, and Arauco. Although we observed a terrace level correlated to MIS-5a in
307 the Marcona area, we excluded this level from the database due to its limited preservation at other locations and lack
308 of chronological constraints. Our assignment of mapped terrace levels to MIS-5c is primarily based on age constraints
309 by Saillard et al. (2011) for the Marcona area and Jara-Muñoz et al. (2015) for the area between 34° and 38°S.
310 However, in order to evaluate the possibility that our correlation with MIS-5c is flawed, we estimated uplift rates for
311 the lower terraces by assigning them tentatively to either MIS-5a or MIS-5c. We interpolated the uplift rates derived
312 from the MIS-5e level at the sites of the lower terraces and compared the differences (Figure 3A). If we infer that
313 uplift rates were constant in time at each site throughout the three MIS-5 substages, the comparison suggests these

lower terrace levels correspond to MIS-5c because of the smaller difference in uplift rate, rather than to MIS-5a (Figure 3B).

A rigorous assessment of marine terrace elevations is crucial for determining accurate vertical deformation rates. Since fluvial degradation and hillslope processes after the abandonment of marine terraces may alter their morphology (Anderson et al., 1999; Jara-Muñoz et al., 2015), direct measurements of terrace elevations at the inner edge (foot of the paleo-cliff) may result in overestimation of the terrace elevations and vertical deformation rates (Jara-Muñoz et al., 2015). To precisely measure the shoreline angle elevations of the MIS 5 terrace level, we used a profile-based approach in TerraceM, a graphical user interface in MATLAB® (Jara-Muñoz et al., 2016), available at www.terracem.com. We placed swath profiles of variable width perpendicular to the previously mapped inner edge, which were used by the TerraceM algorithm to extract maximum elevations to avoid fluvial incision (Fig. 2A and B). For the placement of the swath profiles we tried to capture a local representation of marine terrace topography with a sufficiently long, planar paleo-platform, and a sufficiently high paleo-cliff, simultaneously avoiding topographic disturbance, such as colluvial wedges or areas characterized by river incision. North of Caleta Chañaral (29°S), we used swath profiles of 200 m width, although we occasionally used 100-m-wide profiles for narrow terrace remnants. South of 29°S, we used swath widths of 130 and 70 m. The width was chosen based on fluvial drainage densities that are associated with climate gradients. Sensitivity tests comparing shoreline-angle measurements from different swath widths in the Chala Bay and at Punta Galera show only minimal vertical deviations of less than 0.5 m (Fig. 2E). The sections of these profiles, which represent the undisturbed paleo-platform and paleo-cliff, were picked manually and fitted by linear regression. The extrapolated intersection between both regression lines ultimately determines the buried shoreline-angle elevation and associated uncertainty, which is derived from the 95% confidence interval (2σ) of both regressions (Fig. 2C and D). In total, we measured 1843 MIS 5e and 110 MIS 5c shoreline angle elevations. To quantify the paleo-position of the relative sea-level elevation and the involved uncertainty for the WALIS template, we calculated the indicative meaning using the IMCalc software from Lorscheid and Rovere (2019). The indicative meaning comprises the range between the lower and upper limits of sea-level formation — the indicative range — as well as its mathematically averaged position, which corresponds to the reference water level (Lorscheid and Rovere, 2019).

340
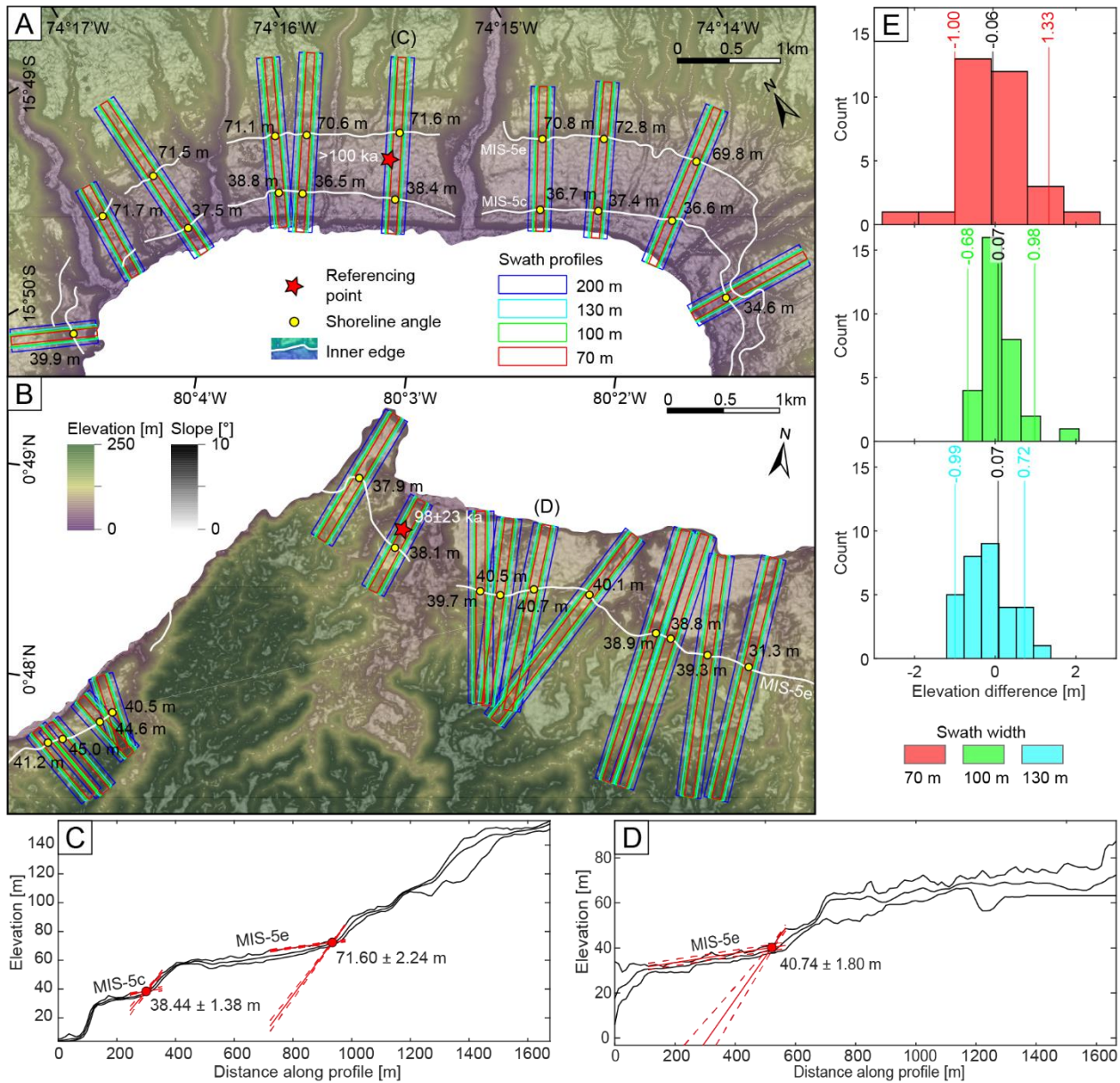
Figure 2. Orthometrically corrected TanDEM-X and slope map of (A) Chala Bay in south-central Peru and (B) Punta
Galera in northern Ecuador with mapped inner shoreline edges of the MIS-5e and 5c terrace levels. Colored rectangles
represent swath-profile boxes of various widths that were placed perpendicular to the inner edges for the subsequent
estimation of terrace elevation in TerraceM. The red star indicates the referencing point with the age constraint for the
respective area (Pedoja et al., 2006b; Saillard, 2008). (C) and (D) Estimation of the shoreline-angle elevation in TerraceM
by intersecting linear-regression fits of the paleo-cliff and paleo-platform (200-m-wide swath profiles). (E) Histograms of
elevation differences measured in both areas for various swath widths (70 m, 100 m, and 130 m) with respect to the 200-m-
wide reference swath profile (blue). Vertical lines indicate median values and standard deviations (2σ).

349

350

351

352

Table 1. Age constraints used for mapping of the inner edge of MIS-5 and for verifying our terrace-elevation measurements. This compilation is mainly based on the terrace catalog of Pedoja et al. (2011); added references include Victor et al. (2011) for Pampa de Mejillones, Martinod et al. (2016b) for northern Chile, and Jara-Muñoz et al. (2015) for south-central Chile. Absolute ages refer to MIS-5e marine terraces, unless otherwise specified; inferred ages refer to their associated MIS. IRSL: Infrared Stimulated Luminescence, AAR: Amino-Acid Racemization, CRN: Cosmogenic Radionuclides, ESR: Electron Spin Resonance.

Country	Location	Lat.	Long.	Dating method	Confidence	Reference	Age [ka]
Ecuador	Galera	0.81	-80.03	IRSL	5	Pedoja et al., 2006b	98±23
Ecuador	Manta	-0.93	-80.66	IRSL, U/Th	5	Pedoja et al., 2006b	76±18, 85±1
Ecuador	La Plata	-1.26	-81.07	U/Th	5	Pedoja et al., 2006b	104±2
Ecuador	Manta	-1.27	-80.78	IRSL	5	Pedoja et al., 2006b	115±23
Ecuador	Santa Elena	-2.21	-80.88	U/Th	5	Pedoja et al., 2006b	136±4, 112±2
Ecuador	Puna	-2.60	-80.40	U/Th	5	Pedoja et al., 2006b	98±3, 95±0
Peru	Cancas	-3.72	-80.75	Morphostratigraphy	5	Pedoja et al., 2006b	~125
Peru	Mancora/ Lobitos	-4.10	-81.05	Morphostratigraphy	5	Pedoja et al., 2006b	~125
Peru	Talara	-4.56	-81.28	Morphostratigraphy	5	Pedoja et al., 2006b	~125
Peru	Paita	-5.03	-81.06	Morphostratigraphy	5	Pedoja et al., 2006b	~125
Peru	Bayovar/ Illescas	-5.31	-81.10	IRSL	5	Pedoja et al., 2006b	111±6
Peru	Cerro Huevo	-15.31	-75.17	CRN	5	Saillard et al., 2011	228±28 (7e)
Peru	Chala Bay	-15.85	-74.31	CRN	5	Saillard, 2008	> 100
Peru	Ilo	-17.55	-71.37	AAR	5	Ortlieb et al., 1996b; Hsu et al., 1989	~125, ~105
Chile	Punta Lobos	-20.35	-70.18	U/Th, ESR	5	Radtke, 1989	~125
Chile	Cobija	-22.55	-70.26	Morphostratigraphy	4	Ortlieb et al., 1995	~125, ~105
Chile	Michilla	-22.71	-70.28	AAR	3	Leonard & Wehmiller, 1991	~125
Chile	Hornitos	-22.85	-70.30	U/Th	5	Ortlieb et al., 1996a	108±1, 118±6
Chile	Chacaya	-22.95	-70.30	AAR	5	Ortlieb et al., 1996a	~125
Chile	Pampa Mejillones	-23.14	-70.45	U/Th	5	Victor et al., 2011	124±3
Chile	Mejillones/ Punta Jorge	-23.54	-70.55	U/Th, ESR	3	Radtke, 1989	~125
Chile	Coloso	-23.76	-70.46	ESR	3	Schellmann & Radtke, 1997	106±3
Chile	Punta Piedras	-24.76	-70.55	CRN	5	Martinod et al., 2016b	138±15
Chile	Esmeralda	-25.91	-70.67	CRN	5	Martinod et al., 2016b	79±9
Chile	Caldera	-27.01	-70.81	U/Th, ESR	5	Marquardt et al., 2004	~125
Chile	Bahia Inglesa	-27.10	-70.85	U/Th, ESR	5	Marquardt et al., 2004	~125
Chile	Caleta Chanaral	-29.03	-71.49	CRN	5	Martinod et al., 2016b	138±0
Chile	Coquimbo	-29.96	-71.34	AAR	5	Leonard & Wehmiller, 1992; Hsu et al., 1989	~125
Chile	Punta Lengua de Vaca	-30.24	-71.63	U/Th	5	Saillard et al., 2012	95±2 (5c)
Chile	Punta Lengua de Vaca	-30.30	-71.61	U/Th	5	Saillard et al., 2012	386±124 (11)
Chile	Quebrada Palo Cortado	-30.44	-71.69	CRN	5	Saillard et al., 2009	149±10

Chile	Rio Limari	-30.63	-71.71	CRN	5	Saillard et al., 2009	318±30 (9c)
Chile	Quebrada de la Mula	-30.79	-71.70	CRN	5	Saillard et al., 2009	225±17 (7e)
Chile	Quebrada del Teniente	-30.89	-71.68	CRN	5	Saillard et al., 2009	678±51 (17)
Chile	Puertecillo	-34.09	-71.94	IRSL	5	Jara-Munoz et al., 2015	87±7 (5c)
Chile	Pichilemu	-34.38	-71.97	IRSL	5	Jara-Munoz et al., 2015	106±9 (5c)
Chile	Putu	-35.16	-72.25	IRSL	5	Jara-Munoz et al., 2015	85±8 (5c)
Chile	Constitucion	-35.40	-72.49	IRSL	5	Jara-Munoz et al., 2015	105±8 (5c)
Chile	Constitucion	-35.44	-72.47	IRSL	5	Jara-Munoz et al., 2015	124±11
Chile	Carranza	-35.58	-72.61	IRSL	5	Jara-Munoz et al., 2015	67±6 (5c)
Chile	Carranza	-35.64	-72.54	IRSL	5	Jara-Munoz et al., 2015	104±9
Chile	Pelluhue	-35.80	-72.54	IRSL	5	Jara-Munoz et al., 2015	112±10
Chile	Pelluhue	-35.80	-72.55	IRSL	5	Jara-Munoz et al., 2015	102±9 (5c)
Chile	Curanipe	-35.97	-72.78	IRSL	5	Jara-Munoz et al., 2015	265±29
Chile	Arauco	-37.62	-73.67	IRSL	5	Jara-Munoz et al., 2015	89±9 (5c)
Chile	Arauco	-37.68	-73.57	CRN	5	Melnick et al., 2009	127±13
Chile	Arauco	-37.71	-73.39	CRN	5	Melnick et al., 2009	133±14
Chile	Arauco	-37.76	-73.38	CRN	5	Melnick et al., 2009	130±13
Chile	Cerro Caleta Curiñanco	-39.72	-73.40	Tephrochronology	4	Pino et al., 2002	~125
Chile	South Curiñanco	-39.76	-73.39	Tephrochronology	4	Pino et al., 2002	~125
Chile	Valdivia	-39.80	-73.39	Tephrochronology	4	Pino et al., 2002	~125
Chile	Camping Bellavista	-39.85	-73.40	Tephrochronology	4	Pino et al., 2002	~125
Chile	Mancera	-39.89	-73.39	Tephrochronology	5	Silva, 2005	~125
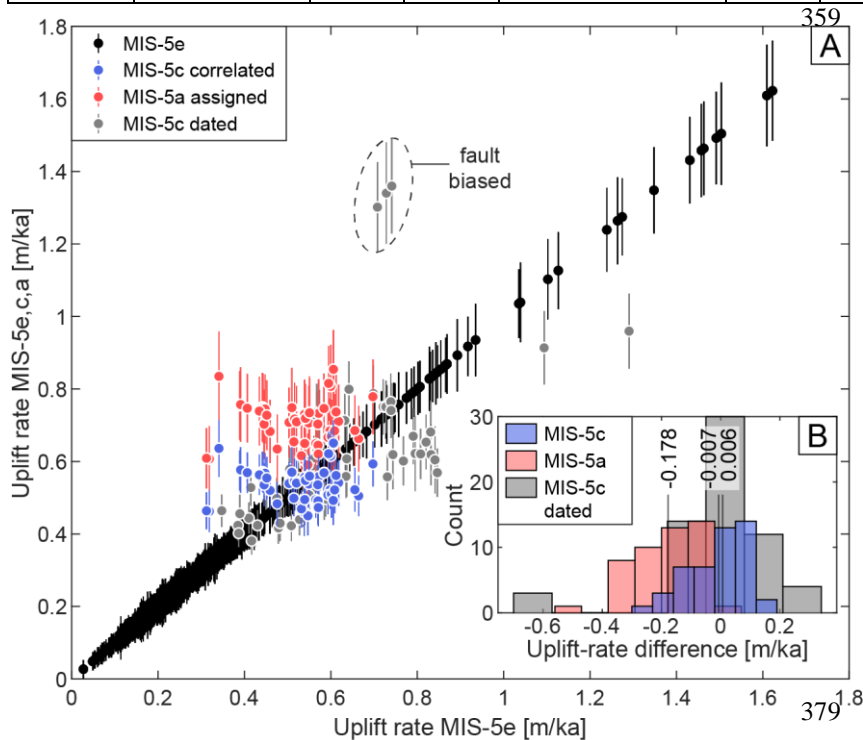
Figure 3. Comparison of MIS-5 uplift-rate estimates. (A) Uplift rates derived by correlating mapped terrace occurrences located immediately below the MIS-5e level to either MIS-5c (blue) or MIS-5a (red) with respect to MIS-5e uplift rates. Marine terraces correlated to MIS-5c by an age constraint are plotted in gray color. (B) Histograms of differences between MIS-5a or MIS-5c uplift rates and MIS-5e uplift rates. Vertical lines show median uplift-rate differences. See section 2.2.2. for relative sea-level elevations of MIS-5a, 5c, 5e.

379

A rigorous assessment of marine terrace elevations is crucial for determining accurate vertical deformation rates. Since fluvial degradation and hillslope processes ~~after the~~subsequent to abandonment of marine terraces may alter ~~their~~ terrace morphology (Anderson et al., 1999; Jara-Muñoz et al., 2015), direct measurements of terrace elevations at the inner edge (foot of the paleo-cliff) may result in overestimation of the terrace elevations and vertical deformation rates (Jara-Muñoz et al., 2015). To precisely measure the shoreline-angle elevations of the MIS-5 terrace level, we used a profile-based approach in TerraceM, a graphical user interface in MATLAB® (Jara-Muñoz et al., 2016); ~~, available at~~ www.terracem.com. We placed swath profiles of variable width perpendicular to the previously mapped inner edge, which were used by the TerraceM algorithm to extract maximum elevations to avoid areas of fluvial incision (Fig. 2A and B). For the placement of the swath profiles we tried to capture a local representation of marine terrace topography with a sufficiently long, planar paleo-platform, and a sufficiently high paleo-cliff, simultaneously avoiding topographic disturbance, such as colluvial wedges or areas ~~characterized by river~~affected by incision. North of Caleta Chañaral (29°S), we used swath profiles of 200 m width, although we occasionally used 100-m-wide profiles for narrow terrace remnants. South of 29°S, we used swath widths of 130 and 70 m. The width was chosen based on fluvial drainage densities that are associated with ~~climate~~precipitation gradients. Sensitivity tests comparing shoreline-angle measurements from different swath widths in the Chala Bay and at Punta Galera show only minimal vertical deviations of less than 0.5 m (Fig. 2E). The sections of these profiles, which represent the undisturbed paleo-platform and paleo-cliff areas, were picked manually and fitted by linear regression. The extrapolated intersection between both regression lines ultimately ~~determines~~allowed us to determine the buried shoreline-angle elevation and associated uncertainty, which is derived from the 95% confidence interval (2σ) of both regressions (Fig. 2C and D). In total, we measured 1843 MIS-5e and 110 MIS-5c shoreline-angle elevations. To quantify the paleo-position of the relative sea-level elevation and the involved uncertainty for the WALIS database, we calculated the indicative meaning for each marine terrace measurement using the IMCalc software from Lorscheid and Rovere (2019). The indicative meaning comprises the range between the lower and upper limits of sea-level formation – the indicative range – as well as its mathematically averaged position, which corresponds to the reference water level (Lorscheid and Rovere, 2019). Table 2 ~~shows~~documents the medians and standard deviations of these values for four extensive regions along the WSAC.

Table 2. Median values and standard deviations (2σ) ~~that~~ representing the indicative meaning along the WSAC. The four sectors were chosen based on their main geomorphic characteristics (see results section).

	Upper limit of modern analog [m]	Lower limit of modern analog [m]	Reference water level [m]	Indicative range [m]
Ecuador and northern Peru	2.89 ± 0.16	-1.78 ± 0.47	0.54 ± 0.21	4.66 ± 0.65
Central and southern Peru	2.98 ± 0.31	-3.05 ± 0.52	-0.03 ± 0.11	6.06 ± 0.90
Northern Chile	3.01 ± 0.15	-2.89 ± 0.30	0.06 ± 0.08	5.90 ± 0.51
Central Chile	3.21 ± 0.19	-3.03 ± 0.38	0.07 ± 0.11	6.25 ± 0.60

410   To quantify the reliability and consistency of our shoreline-angle measurements, we developed a quality rating from

411   low (1) to high (5) confidence. Equation 1 illustrates how we calculated the individual parameters and the overall

412   quality rating:

413   **Equation 1: Quality rating.**

414
$$QR = 1 + 2.4 * \left(\frac{C_{RP}}{\max(C_{RP})} * \left(1 - \frac{D_{RP}}{\max(D_{RP})} \right) \right)^{e} + 1.2 * \left(1 - \frac{E_T}{\max(E_T)} \right) + 0.4 * 1.2 * \left(1 - \frac{R}{\max(R)} \right)$$

415   The four parameters ~~that we~~ included in our quality rating (QR) comprise a) the distance to the nearest referencing

416   point (D_{RP}), b) the confidence of the referencing point ~~that is~~ based on the dating method used by previous studies

417   (C_{RP}) (Pedoja et al., 2011), c) the measurement error in TerraceM (E_T), and (d) the pixel-scale resolution of the

418   topographic data set (R) (Fig. 4). We did not include the error that results from the usage of different swath widths,

419   since the calculated elevation difference with respect to the most frequently used 200 m swath width is very low (<

420   0.5 m) (Fig. 2E). From the reference points we only used data points with a confidence value of 3 or greater (1 – poor,

421   5 – very good) based on the previous qualification of Pedoja et al. (2011). The confidence depends mainly on the

422   reliability of the dating method, but can be increased by good age constraints of adjacent terrace levels or detailed

423   morphostratigraphic correlations, such as in Chala Bay (Fig. 2A) (Goy et al., 1992; Saillard, 2008). We further used

424   this confidence value to quantify the quality of the age constraints in the WALIS template.

425   To account for the different uncertainties of the individual parameters in the QR, we combined and weighted the

426   parameters D_{RP} and C_{RP} in a first equation claiming 60% of the final QR, E_T in a second and R in a third equation

427   weighted 30% and 10%, respectively. We justify these percentages by the fact that the distance and confidence to the

428   nearest referencing point is of utmost importance for identifying the MIS-5e terrace level. The measurement error

429   represents how well the mapping of the paleo-platform and paleo-cliff resulted in the shoreline-angle measurement,

430   while the topographic resolution of the underlying DEM only influences the precise representation of the actual

431   topography and has little impact on the measurement itself. The coefficient assigned to the topographic resolution is

432   multiplied by a factor of 1.2 in order to maintain the possibility of a maximum QR for a DEM resolution of 5 m.

433   Furthermore, we added an exponent to the first part of the equation to reinforce low confidence and/or high distance

434   of the referencing point for low quality ratings. The exponent adjusts the QR according to the distribution of distances

435   from referencing points, which follows an exponential relationship (Fig. 4D).

436   The influence of each parameter to the quality rating can be observed in Fig. 4. We observe that for high D_{RP} values

437   the QR becomes constant; likewise, the influence of QR parameters becomes significant for QR values higher than 3.

438   We justify the constancy of the QR for high D_{RP} values (> 300 km) by the fact that most terrace measurements have

439   D_{RP} values below 200 km (Fig. 4D). The quality rating is then used as a descriptor of the confidence of marine terrace-

440   elevation measurements.
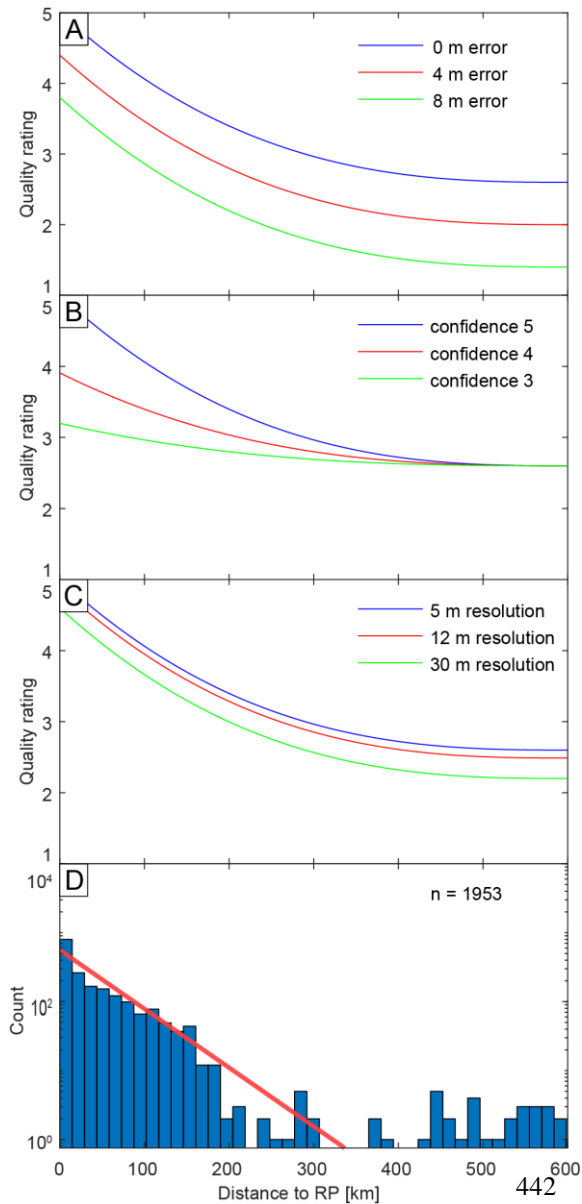
Figure 4. Influence of the parameters on the quality rating. The x-axis is the distance to reference point (RP), the y-axis is the quality rating, the color lines represent different values of quality rating parameters. While one parameter is being tested, the remaining parameters are set to their best values. That is why the QR does not reach values of 1 in the graphs displayed here. (A) Shoreline-angle elevation error. (B) Confidence value of the referencing point. (C) Topographic resolution of the DEM used for terrace-elevation estimation. (D) Histogram displaying the distribution of distances between each shoreline-angle measurement and its nearest RP (n: number of measurements). The red line is an exponential fit.

442

3.2. Estimating coastal uplift rates

Uplift-rate estimates from marine terraces *(u)* were calculated using equations 2 and 3:

Equation 2: Relative sea level.

$$\Delta H = H_T - H_{SL}$$

Equation 3: Uplift rate.

$$u = \frac{H_T - H_{SL}}{T}$$

449 where ΔH is the relative sea level, H_{SL} is the sea-level altitude of the interglacial maximum, H_T is the shoreline-angle

450 elevation of the marine terrace, and T its associated age (Lajoie, 1986).

451 We calculated the standard error $SE(u)$ using equation 4 from Gallen et al. (2014):

452 **Equation 4: Uplift-rate error.**

$$SE(u)^2 = u^2\left(\left(\frac{\sigma_{\Delta H}^2}{\Delta H^2}\right) + \left(\frac{\sigma_T^2}{T^2}\right)\right)$$

454 where $\sigma_{\Delta H}^2$, the error in relative sea level, equals ($\sigma_{H_T}^2 + \sigma_{H_{SL}}^2$). The standard-error estimates comprise the uncertainty

455 in shoreline-angle elevations from TerraceM (σ_{H_T}), error estimates in absolute sea level ($\sigma_{H_{SL}}$) from Rohling et al.

456 (2009), and an arbitrary range of 10 ka for the duration of the highstand (σ_T).

457 Vertical displacement rates and relative sea level are influenced by flexural rebound associated with loading and

458 unloading of ice sheets during glacio-isostatic adjustments (GIA) (Stewart et al., 2000; Shepherd and Wingham, 2007).

459 The amplitude and wavelength of GIA is mostly determined by the flexural rigidity of the lithosphere (Turcotte and

460 Schubert, 1982) and should therefore not severely influence vertical deformation along non-glaciated coastal regions

461 (Rabassa and Clapperton, 1990) that are located in the forearc of active subduction zones. This is supported by

462 Creveling et al. (2017) by showingwho showed no significant GIA along the WSAC between 1°N and 40°S since

463 MIS-5a. Current GIA models use an oversimplified lithospheric structure defined by horizontal layers of

464 homogeneous rheology (e.g., Creveling et al., 2017), which might be appropriate for cratons and ocean basins, but not

465 necessarily alongfor the forearcs of subduction zonesmargins. Therefore, Because of their intrinsic modeling

466 complexities, we did not account for the GIA effect on terrace elevations and uplift rates.

467 **3.3.   Tectonic parameters of the South American convergent margin**

468 We compared the deformation patterns of marine terraces along the coast of South America with proxies that included

469 crustal faults, bathymetric anomalies, trench-sediment thickness, and distance to the trench. To evaluate the possible

470 control of climatic parameters in the morphology of marine terraces, we compared our data set with wave heights,

471 tidal range, mean annual precipitation rate, and the azimuth of the coastline (Schweller et al., 1981; Bangs and Cande,

472 1997; von Huene et al., 1997; Collot et al., 2002; Ceccherini et al., 2015; Hayes et al., 2018; Santibáñez et al., 2019;

473 GEBCO Bathymetric Compilation Group, 2020) (Fig. 1).

474 To evaluate the potential correlations between tectonic parameters and marine terraces, we analyzed the latitudinal

475 variability of these parameters projected along a curved "simple profile" and a 300-km-wide "swath profile" following

476 the trace of the trench. We used simple profiles for visualizing 2D data sets; for instance, to compare crustal faults

477 along the forearc area of the margin (Veloza et al., 2012; Melnick et al., 2020), we projected the seaward tip of each

478 fault. For the trench-sediment thickness, we projected discrete thickness estimates based on measurements from

479 seismic reflection profiles of Bangs and Cande (1997), Collot et al. (2002), Huene et al. (1996), and Schweller et al.

480 (1981). Finally, we projected the discrete trench distances from the point locations of our marine terrace measurements

481 along a simple profile. To compare bathymetric features on the oceanic plate, we used a compilation of bathymetric
482 measurements at 450 m resolution (GEBCO Bathymetric Compilation Group, 2020). The data set was projected along
483 a curved, 300-km-wide swath profile using TopoToolbox (Schwanghart and Kuhn, 2010).

484 Finally, to elucidate the influence of climatic factors on marine terrace morphology, we compared the elevation, but
485 also the number of measurements as a proxy for preservation and exposure of marine terraces. We calculated wave
486 heights, tidal ranges, and reference water levels at the point locations of our marine terrace measurements using the
487 Indicative Meaning Calculator (IMCalc) from Lorscheid and Rovere (2019). We used the maximum values of the
488 hourly significant wave height, and for the tidal range we calculated the difference between the highest and lowest
489 astronomical tide. The reference water level represents the averaged position of the paleo sea level with respect to the
490 shoreline-angle elevation and, together with the indicative range (uncertainty), quantifies the indicative meaning
491 (Lorscheid and Rovere, 2019). We furthermore used the high-resolution data set of Ceccherini et al. (2015) for mean
492 annual precipitation, and we compared the azimuth of the coast in order to evaluate its exposure to wind and waves.
493 To facilitate these comparisons, we extracted the values of all these parameters at the point locations of our marine
494 terrace measurements and projected them along a simple profile. Calculations and outputs were processed and
495 elaborated using MATLAB® 2020b.

496 **4.   Results**

497 **4.1.   Marine terrace geomorphology and shoreline-angle elevations**

498 In the following sections we describe our synthesized database of last interglacial marine terrace elevations along the
499 WSAC. Marine terraces of the last interglacial are generally well preserved and almost continuously exposed along
500 the WSAC, allowing to the estimateion of elevations with a high spatial density. To facilitate the descriptions of
501 marine terrace-elevation patterns, we divided the coastline into four sectors based on their main geomorphic
502 characteristics (Fig. 5): 1) the Talara bend in northern Peru and Ecuador, 2) southern and central Peru, 3) northern
503 Chile, and 4) central and south-central Chile. In total we carried out 1,843 MIS-5e terrace measurements with a median
504 elevation of 30.1 m asl and 110 MIS-5c terrace measurements with a median of 38.6 m. The regions with exceptionally
505 high marine terrace elevations (≥ 100 m) comprise the Manta Peninsula in Ecuador, the San Juan de Marcona area in
506 south-central Peru, and three regions in south-central Chile (Topocalma, Carranza, and Arauco). Marine terraces at
507 high altitudes (≥ 60 m) can also be found in Chile on the Mejillones Peninsula, south of Los Vilos, near Valparaíso,
508 in Tirua, and near Valdivia, while terrace levels only slightly above the median elevation are located at Punta Galera
509 in Ecuador, south of Puerto Flamenco, at Caldera/Bahía Inglesa, near Caleta Chañaral, and near the Quebrada El
510 Moray in the Altos de Talinay area in Chile. In the following sections we describe the characteristics of each site in
511 detail, the names of the sites are written in brackets following the same nomenclature as in the WALIS database (i.e.,
512 Pe – Peru, Ec – Ecuador, Ch – Chile).

513
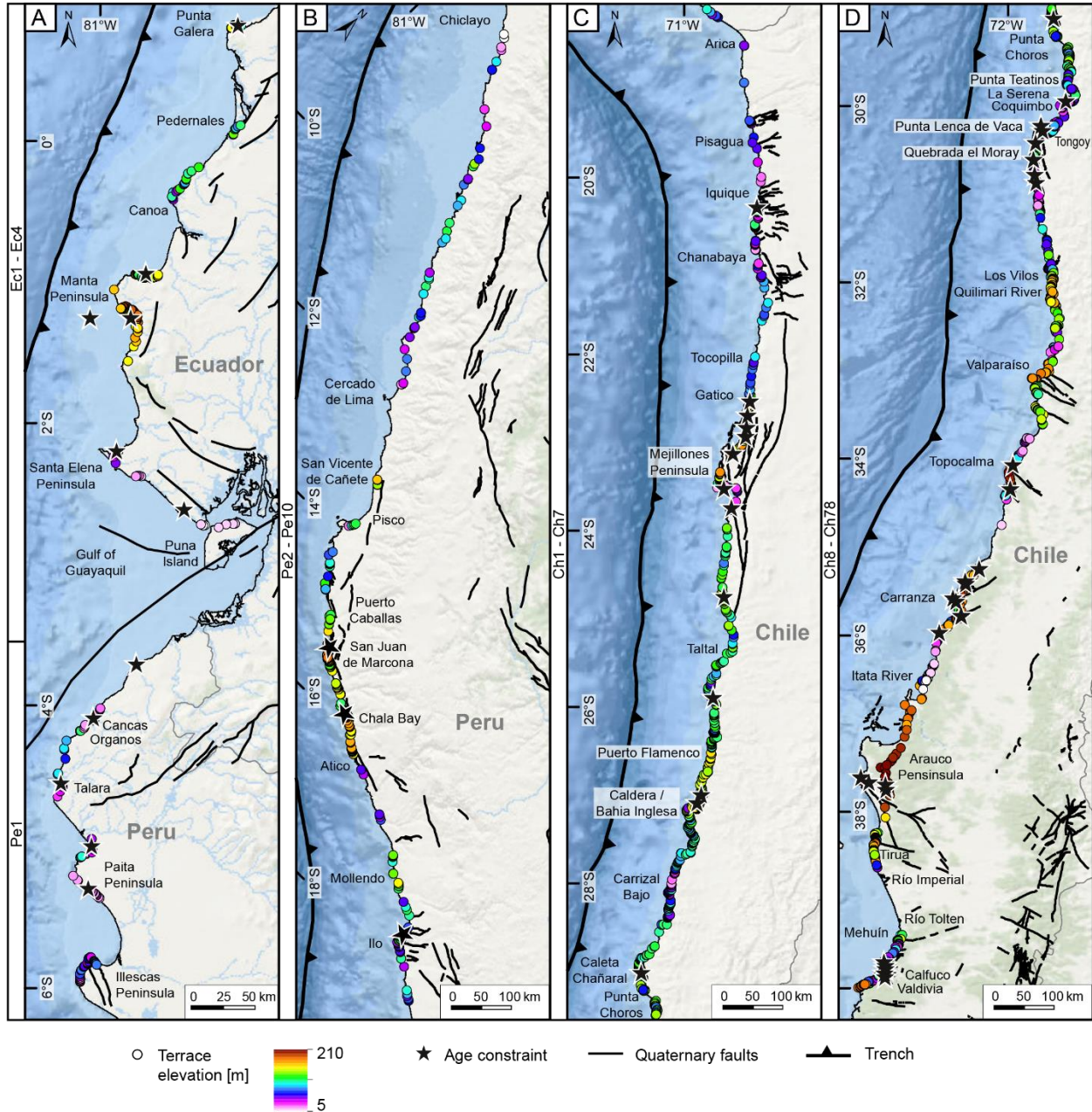
Figure 5. Shoreline-angle elevation measurements (colored points), referencing points (black stars), Quaternary faults (bold black lines) (Veloza et al., 2012; Melnick et al., 2020), and locations mentioned in the text for the four main geomorphic segments (for location see Fig. 1A) (World Ocean Basemap: Esri, Garmin, GEBCO, NOAA NGDC, and other contributors). Site names referring to the entries in the WALIS database are on the left margin of each sub-figure (Pe – Peru, Ec – Ecuador, Ch – Chile). (A) Talara bend in Ecuador and northern Peru. (B) Central and southern Peru. (C) Northern Chile. (D) Central and south-central Chile.

4.1.1.   Ecuador and northern Peru (1°N–6.5°S)

The MIS-5e terrace levels in Ecuador and northern Peru [sites Ec1 to Ec4 and Pe1] are discontinuously preserved along the coast (Fig. 6). They often occur at low elevations (between 12 m and 30 m) and show abrupt local changes

523 in elevation, reaching a maximum at the Manta Peninsula. Punta Galera in northern Ecuador displays relatively broad

524 and well-preserved marine terraces ranging between 40 and 45 m elevation and rapidly decrease eastward to about 30

525 m asl across the Cumilínche fault [Ec1]. Farther south, between Pedernales and Canoa [Ec1], narrow terraces occur

526 at lower altitudes of 22–34 m asl. A long-wavelength (~120 km) pattern in terrace-elevation change can be observed

527 across the Manta Peninsula with the highest MIS-5e terraces peaking at ~100 m asl at its southern coast [Ec2]. This

528 terrace level is hardly visible in its highest areas with platform widths smaller than 100 m due to deeply incised and

529 narrowly spaced river valleys. We observe lower and variable elevations between 30 and 50 m across the Rio Salado

530 fault in the San Mateo paleo-gulf in the north, while the terrace elevations increase gradually from ~40 m in the Pile

531 paleo-gulf in the south [Ec3] toward the center of the peninsula (El Aromo dome) and the Montecristi fault [Ec3]. A

532 lower terrace level correlated to MIS-5c displays similar elevation patterns as MIS-5e within the Pile paleo-gulf and

533 areas to the north. Near the Gulf of Guayaquil and the Dolores-Guayaquil megashear, the lowest terrace elevations

534 occur at the Santa Elena Peninsula ranging between 17 and 24 m asl and even lower altitudes in its southern part, and

535 on the Puna Island ranging between 11 and 16 m asl [Ec4]. In northern Peru [Pe1], we observe dismembered MIS-5e

536 terraces in the coastal area between Cancas and Talara below the prominent Mancora Tablazo. "Tablazo" is a local

537 descriptive name used in northern Peru (~3.5–6.5°S) for marine terraces that cover a particularly wide surface area

538 (Pedoja et al., 2006b). South of Cancas, MIS-5e terrace elevations range between 17 and 20 m asl, reaching 32 m near

539 Organos, and vary between 20 and 29 m in the vicinity of Talara. In the southward continuation of the Talara harbor,

540 the Talara Tablazo widens, with a lower marine terrace at about 23 m asl immediately north of Paita Peninsula reaching

541 30 m asl in the northern part of the peninsula. The last occurrence of well-preserved MIS-5e terraces in this sector

542 exists at the Illescas Peninsula, where terrace elevations decrease from around 30 m to 17 m asl southward.
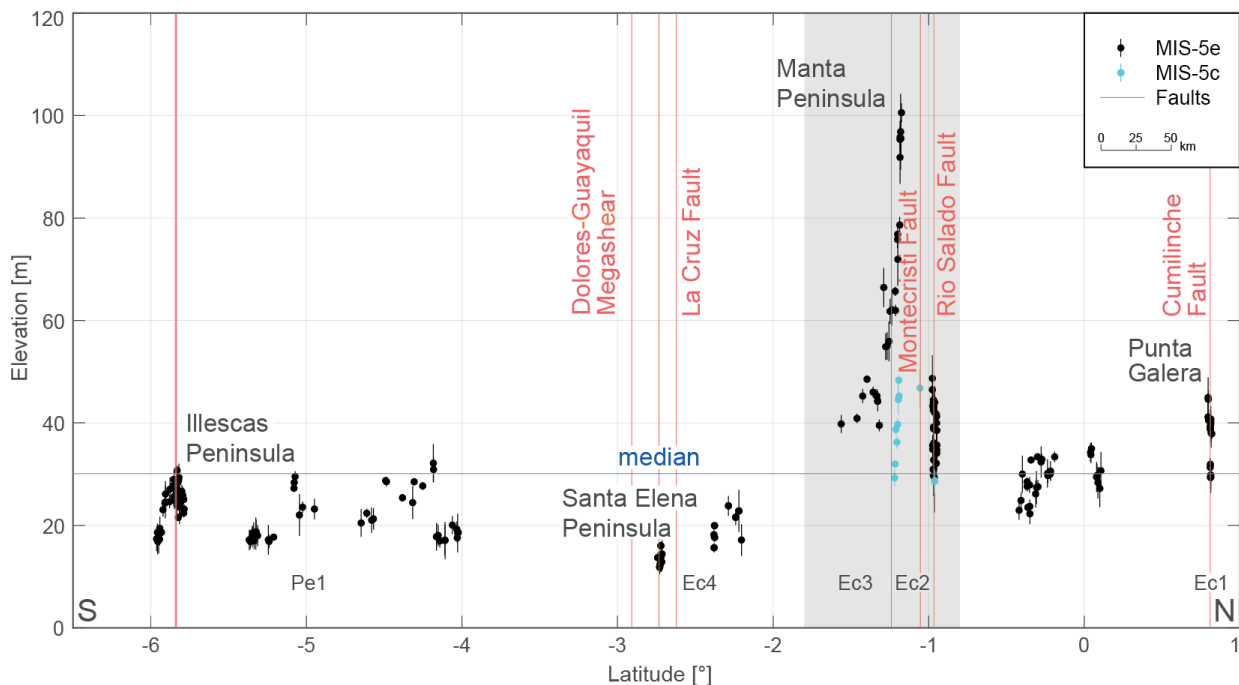
543
544 **Figure 6. Measured shoreline-angle elevations of MIS-5e and 5c in Ecuador (Ec) and northern Peru (Pe). A high and**
545 **inferred long-wavelength change in terrace elevation occurs at the Manta Peninsula (gray area) and at low elevations**

546 **farther south at the Santa Elena Peninsula. Several terrace-elevation changes over short distances coincide with faulting at**
547 **Punta Galera and on the Illescas Peninsula. Median elevation: 30.1 m. For location see Fig. 5A.**

548 ### 4.1.2.   Central and southern Peru (6.5°–18.3°S)

549 This segment comprises marine terraces at relatively low and constant elevations, but which are rather discontinuous
550 [sites Pe2 to Pe10], except in the San Juan de Marcona area, where the terraces increase in elevation drastically (Fig.
551 7). The coast in north-central Peru exhibits poor records of MIS-5e marine terraces, characterized by mostly narrow
552 and discontinuous remnants that are sparsely distributed along the margin with limited age constraints. Marine terraces
553 increase in elevation from 11 to 35 m asl south of Chiclayo [Pe2] and decrease to 17 m asl near Cercado de Lima [Pe3,
554 Pe4], forming a long-wavelength (~600 km), small amplitude (~20 m) upwarped structure. The MIS-5e terrace levels
555 are better expressed in the south-central and southern part of Peru at elevations between 35 and 47 m asl in San Vicente
556 de Cañete, decreasing to approximately 30 m asl in the vicinity of Pisco [Pe5]. South of Pisco, the coastal area becomes
557 narrow with terrace elevations ranging between 25 and 34 m asl [Pe6] and increasing abruptly to 74–79 m near Puerto
558 Caballas and the Río Grande delta. MIS-5e terrace elevations are highest within the San Juan de Marcona area,
559 reaching 109–93 m at Cerro Huevo and 87–56 m at Cerro Trés Hermanas [Pe7]. These higher terrace elevations
560 coincide with a wider coastal area, a better-preserved terrace sequence, and several crustal faults, such as the San Juan
561 and El Huevo faults.

562 Terrace heights west of Yauca indicate a further decrease to 50–58 m before a renewed increase to 70–72 m can be
563 observed in the Chala embayment [Pe8]. We observe a similar trend in elevation changes for the shoreline angles
564 attributed to the MIS-5c interglacial within the previously described high-elevation area: 31–39 m near the Río Grande
565 delta, 62–58 m below the Cerro Huevo peak, 64–27 m below the Cerro Trés Hermanas peak [Pe7], 36–40 m near
566 Yauca, and 34–40 m within the Chala embayment [Pe8]. Besides various changes in between, terrace elevations
567 decrease slowly from 54 m south of the Chala region to 38 m near Atico [Pe8]. The overall decrease south of the San
568 Juan de Marcona area therefore contrasts strikingly with the sharper decrease to the north. These high-elevation marine
569 terraces, which extend ~250 km along the coast from north of the San Juan de Marcona area to south of Chala Bay,
570 constitute one of the longest wavelength structures of the WSAC. Southeast of Atico, less well-preserved marine
571 terraces appear again in form of small remnants in a narrower coastal area. Starting with elevations as low as 24 m,
572 MIS-5e terrace altitudes increase southeastward to up to 40 m near Mollendo [Pe9], before they slightly decrease
573 again. The broader and quite well-preserved terraces of the adjacent Ilo area resulted in a smooth increase from values
574 greater than 25 m to 33 m and a sudden decrease to as low as 22 m across the Chololo fault [Pe9]. North of the Arica
575 bend, shoreline-angle measurements yielded estimates of 24–29 m in altitude [Pe10].
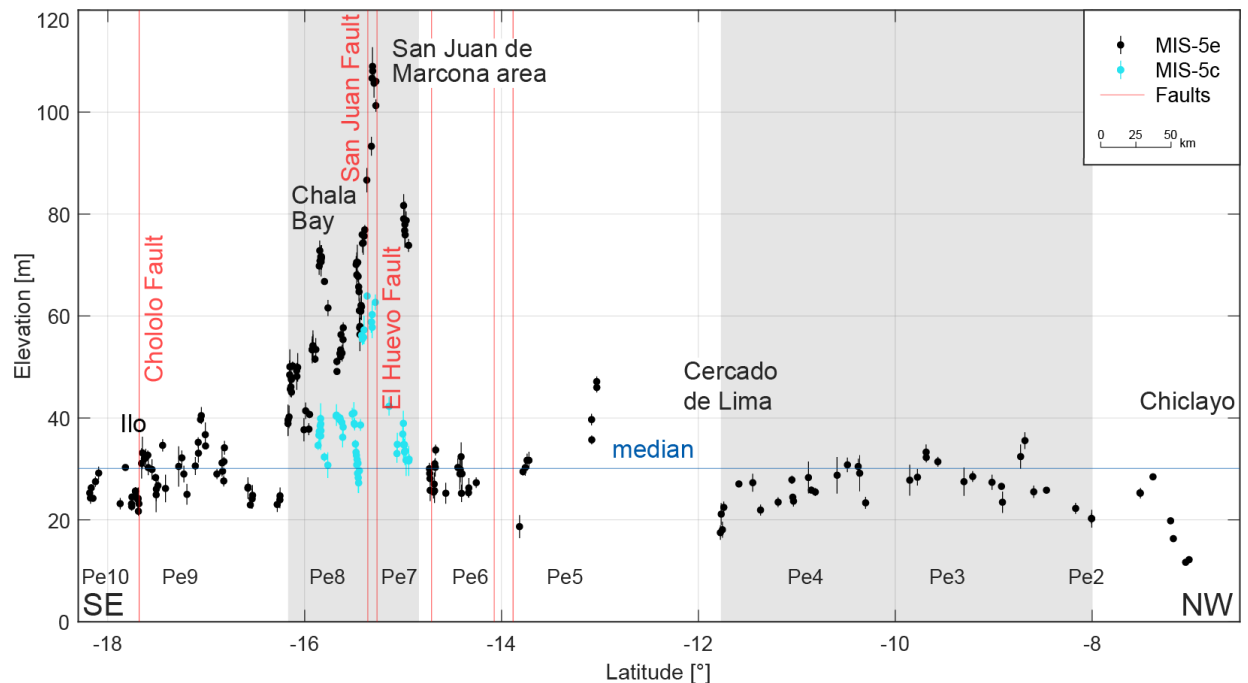
Figure 7. Measured shoreline-angle elevations of MIS-5e and 5c terraces in central and southern Peru (Pe). While only sparsely preserved terraces below the median (30.1 m) occur in central Peru between Chiclayo and Lima, a relatively broad and asymmetric distribution of marine terraces characterizes the area of San Juan de Marcona. For location see Fig. 5B.

4.1.3. Northern Chile (18.3°–29.3°S)

Along the northern Chilean coast, marine terraces of the MIS-5e are characterized by a variable elevation pattern and the occurrence of numerous crustal faults associated with the Atacama fault system, although the changes in terrace elevation are not as pronounced as in the northern segments (Fig. 8) [sites Ch1 to Ch7]. The local widening of the coastal area near the Arica bend narrows southward with MIS-5e terraces at elevations of between 24 and 28 m asl in northernmost Chile [Ch1]. Just north of Pisagua, we measured shoreline-angle elevations of well-preserved marine terraces between 19 and 26 m across the Atajana fault [Ch1]. An areally limited zigzag pattern starting with shoreline-angle elevation values of 32 m south of Iquique and south of the Zofri and Cavancha faults decreases rapidly to approximately 22 m, but increases again to similar altitudes and drops as low as 18 m toward Chanabaya south of the Barranco Alto fault [Ch1]. A gentle, steady rise in terrace elevations can be observed south of Tocopilla where altitudes of 25 m are attained. South of Gatico, terrace markers of the MIS-5e highstand increase and continue northward for much of the Mejillones Peninsula within an approximate elevation range of 32–50 m asl, before reaching a maximum of 62 m asl at the Pampa de Mejillones [Ch2]. With its ~100 km latitudinal extent, we consider this terrace-elevation change to be a medium-wavelength structure. Although no MIS-5e terrace levels have been preserved at the Morro Mejillones Horst (Binnie et al., 2016), we measured shoreline-angle elevations at the elevated southwestern part of the peninsula that decrease sharply from 55 to 17 m asl in the vicinity of the Mejillones fault system [Ch2]. After a short interruption of the MIS-5e terrace level at Pampa Aeropuerto, elevations remain relatively low between 19–25 m farther south [Ch2]. Along the ~300-km coastal stretch south of Mejillones, marine terraces are scattered along the narrow coastal area ranging between 25 and 37 m asl [Ch3]. South of Puerto Flamenco, MIS-5e

599 terrace elevations range between 40 and 45 m asl until Caldera and Bahía Inglesa [Ch4]. The MIS-5e marine terrace
600 elevations decrease abruptly south of the Caldera fault and the Morro Copiapó (Morro Copiapó fault) to between 25
601 and 33 m asl, reaching 20 m asl north of Carrizal Bajo [Ch4]. In the southernmost part of the northern Chilean sector,
602 the MIS-5e terraces rise from around 30 m asl to a maximum of 45 m asl near the Cabo Leones fault [Ch4], before
603 decreasing in elevation abruptly near Caleta Chañaral and Punta Choros [Ch5, Ch6, Ch7].
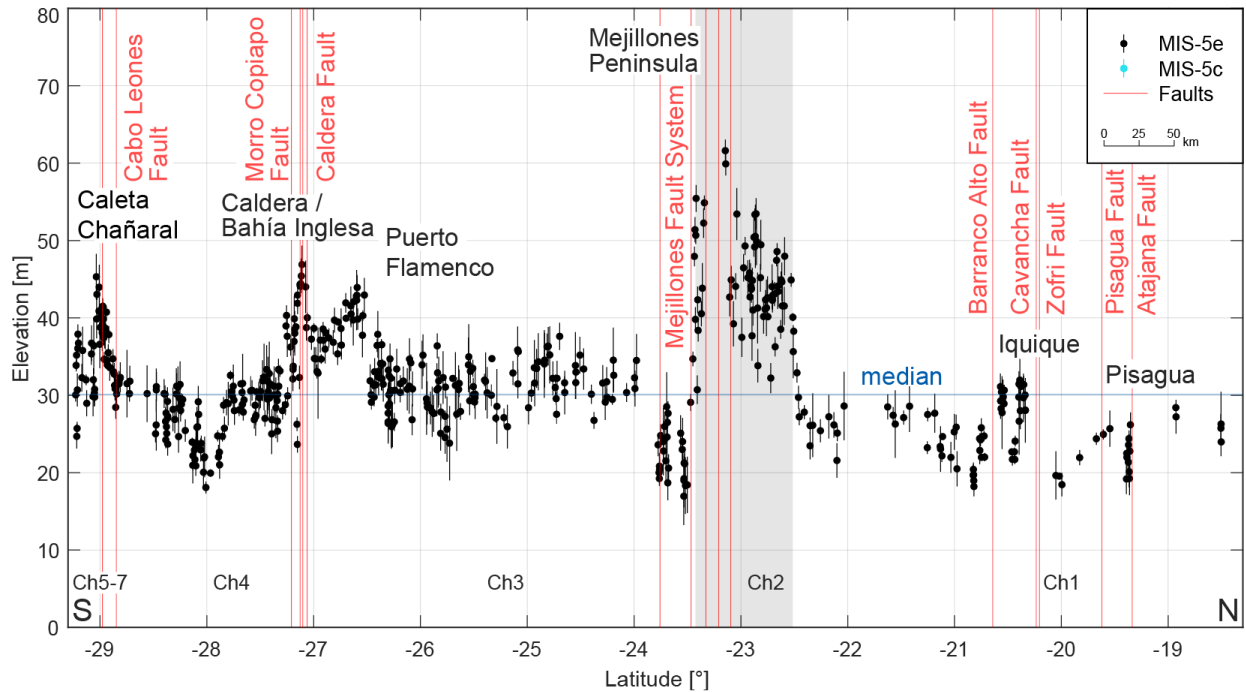
604
605 **Figure 8. Measured shoreline-angle elevations of MIS-5e and 5c terraces in northern Chile (Ch). Faults and asymmetrically**
606 **uplifted marine terraces of up to 60 m elevation characterize the Mejillones Peninsula, reaching values below 20 m at the**
607 **southern margin. Terrace elevations attain peak values south of Puerto Flamenco, at Caldera/Bahía Inglesa, and north of**
608 **Caleta Chañaral, while in between minimum elevations below 20 m prevail (north of Carizal Bajo). Median elevation is**
609 **30.1 m. For location see Fig. 5C.**

610 **4.1.4.   Central Chile (29.3°–40°S)**

611 Marine terraces along central Chile display variable, high-amplitude terrace-elevation patterns associated with
612 numerous crustal faults, and include a broad-scale change in terrace altitudes with the highest MIS-5e marine terrace
613 elevations of the entire South American margin on the Arauco Peninsula (Fig. 9) [sites Ch8 to Ch78]. South of Punta
614 Choros, marine terrace elevations decrease from values close to 40 to 22 m asl north of Punta Teatinos [Ch8, Ch9]. A
615 maximum elevation of 40 m is reached by the terraces just south of this area [Ch10] whereas north of La Serena, a
616 sharp decrease leads to values between 20 and 30 m for marine terraces south of Coquimbo Bay and in the Tongoy
617 Bay area [Ch11, Ch12]. South of Punta Lengua de Vaca, our measurements of the exceptionally well-preserved
618 staircase morphology of the terraces are within the same elevation range between 20 and 30 m, increasing slowly to
619 40 m near the Quebrada el Moray [Ch13]. Although we could not observe a significant change in terrace elevation
620 across the Puerto Aldea fault, we measured an offset of ~7 m across the Quebrada Palo Cortado fault. MIS-5e terrace
621 levels decrease thereafter and vary between 20 and 30 m in altitude until north of Los Vilos [Ch14–Ch18], where they
622 increase in elevation [Ch19], reaching 60 m near the Rio Quilimari [Ch20]. The marine terraces become wider in this

area and are associated with scattered sea stacks. Decreasing farther south to only 20 m asl [Ch21–Ch25], the coastal area narrows and has terrace heights of up to 64 m near Valparaíso, in an area that is cut by numerous faults (e.g., Valparaíso and Quintay faults) [Ch26–Ch32]. Another low-elevation area follows southward, with values as low as 17 m [Ch33–Ch35]. Farther south, between 34°S and 38°S, broad (~200 km at Arauco), medium (~45 km at Topocalma), and narrow (Carranza) upwarped zones occur that are manifested by variable terrace elevations. These include prominent high-terrace elevations at Topocalma with a maximum of 180 m [Ch36–Ch39], slightly lower levels of 110 m at Carranza [Ch42–Ch47], exceptionally low values near the Río Itata (< 10 m) [Ch48–Ch64, Ch66], and the most extensive and highest shoreline-angle elevations on the Arauco Peninsula with elevations in excess of 200 m [Ch67–Ch73]. Additionally, we measured MIS-5c terrace elevations in the three higher exposed areas with a range of 20–55 m at Carranzo, and a few locations at Topocalma (76–81 m) and Arauco (117–123 m). The medium-wavelength structure of Topocalma is bounded by the Pichilemu and Topocalma faults, and near Carranza several fault offsets (e.g., Pelluhue and Carranza faults) are responsible for the short-wavelength changes in terrace elevation. In contrast, crustal faulting is nearly absent in the high-elevation and long-wavelength structure at Arauco. MIS-5e terrace elevations are highly variable within a short area south of the Arauco Peninsula near the Tirua fault, increasing rapidly from 27 m to 78 m and decreasing thereafter to approximately 20 m [Ch74, Ch75]. The continuity of terraces is interrupted by the absence of terrace levels between Río Imperial and Río Toltén, but resumes afterward with a highly frequent zigzag pattern and multiple faults (e.g., Estero Ralicura and Curinanco faults) from as low as 18 m to a maximum of 40 m [Ch76, Ch77]. In this area locations with the highest terrace levels comprise the terraces near Mehuín and Calfuco. A final increase in shoreline-angle elevations from about 20–30 m up to 76 m near Valdivia coincides with the southern terminus of our terrace-elevation measurements [Ch78].
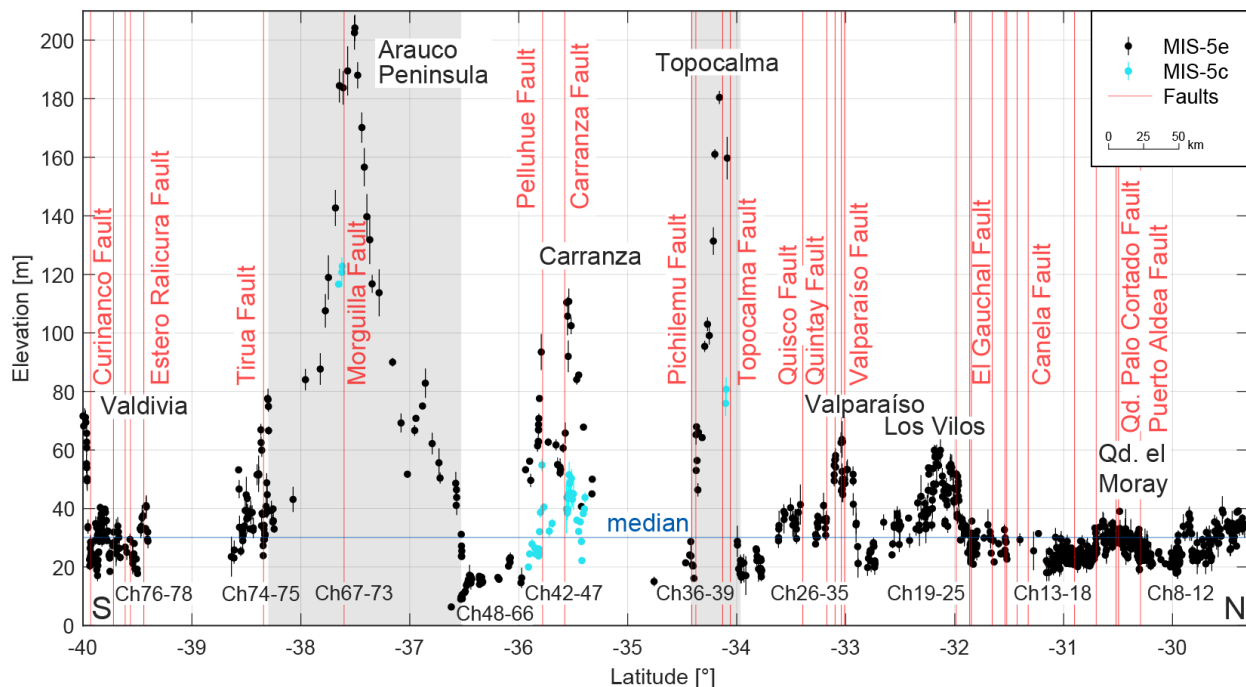
Figure 9. Measured shoreline-angle elevations of MIS-5e and 5c terraces in central Chile (Ch). Extensive faulting coincides with various high terrace elevations of the last interglacial highstand north of Los Vilos, near Valparaiso, at Topocalma, Carranza, and near Valdivia. The most pronounced and long-wavelength change in terrace elevation occurs on the Arauco

647 **Peninsula with maximum elevations over 200 m and minimum elevations below 10 m north of Concepción. Qd. – Quebrada.**
648 **Median elevation: 30.1 m. For location see Fig. 5D.**

649 ## 4.2.   Statistical analysis

650 Our statistical analysis of mapped shoreline-angle elevations resulted in a maximum kernel density at 28.96 m with a

651 95% confidence interval from 18.59 m to 67.85 m (2σ) for the MIS-5e terrace level (Fig. 10A). The MIS-5c terrace

652 yielded in a maximum kernel density at a higher elevation of 37.20 m with 2σ ranging from 24.50 m to 63.92 m. It is

653 important to note that the number of MIS-5c measurements is neither as high nor as continuous as compared to that

654 of the MIS-5e level. MIS-5c data points were measured almost exclusively in sites where MIS-5e reach high elevations

655 (e.g., San Juan de Marcona with MIS-5e elevations between 40 and 110 m).

656 The distribution of measurement errors was studied using probability kernel-density plots for each topographic

657 resolution (1-5 m LIDAR, 12 m TanDEM-X, and 30 m TanDEM-X). The three data sets display similar distributions

658 and maximum likelihood probabilities (MLP); for instance, LiDAR data show a MLP of 0.93 m, the 12 m TanDEM-

659 X a MLP of 1.16 m, and 30 m TanDEM-X a MLP of 0.91 m (Fig. 10B). We observe the lowest errors from the 30 m

660 TanDEM-X, slightly higher errors from the 1-5 m LiDAR data, and the highest errors from the 12 m TanDEM-X.

661 This observation is counterintuitive as we would expect lower errors for topographic data sets with higher resolution

662 (1-5 m LiDAR). The reason for these errors is probably related to the higher number of measurements using the 12 m

663 TanDEM-X (1564) in comparison with the measurements using 30 m TanDEM-X (50), which result in a higher

664 dispersion and a more realistic representation of the measurement errors (Fig. 10B). In addition, the relation between

665 terrace elevations and error estimates shows that comparatively higher errors are associated with higher terrace

666 elevations, although the sparse point density of high terrace-elevation measurements prevents recognition of a clear

667 correlation from being recognized (Fig. 10C).
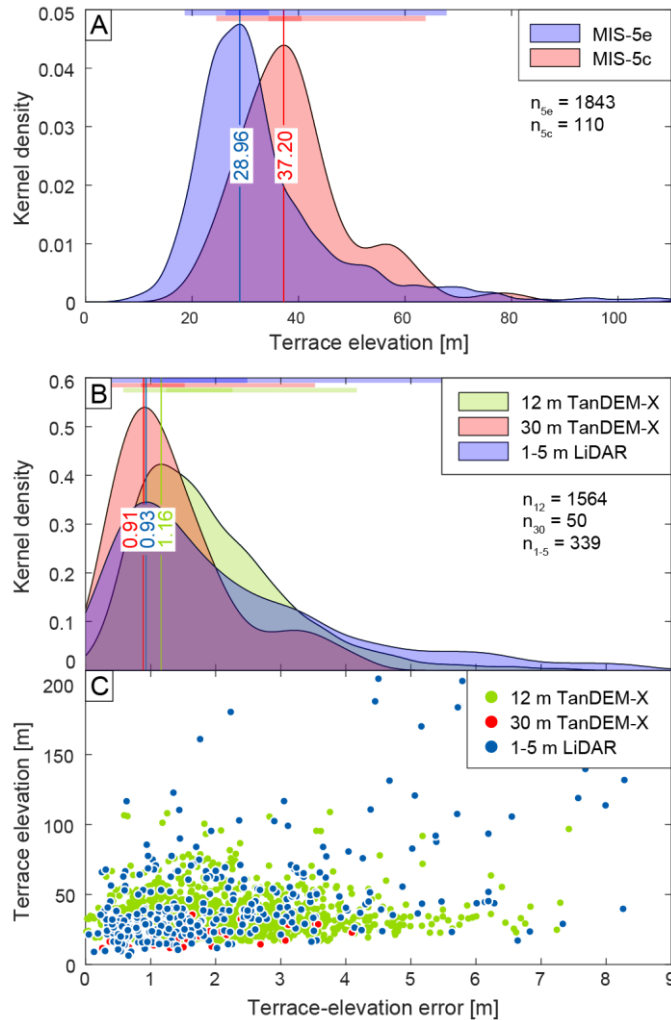
Figure 10. Statistical analysis of measured shoreline-angle elevations. (A) Kernel-density plot of MIS-5e and 5c terrace elevations with maximum likelihood probabilities (m.l.p.) at 28.96 m elevation for MIS-5e and 37.20 m elevation for MIS-5c (n: number of measurements). Colored bars on top highlight the standard deviations σ and 2σ. (B) Kernel-density and their associated standard-deviation (σ and 2σ) calculations of terrace-elevation errors for source DEMs of various resolutions. The most abundant 12 m TanDEM-X has a m.l.p.-error of 1.16 m, while the 30 m TanDEM-X and the 1-5 m LIDAR produce slightly lower errors of 0.91 m and 0.93 m, respectively. (C) Terrace-elevation errors plotted against terrace elevation for the individual source DEMs. Although the point density for high terrace elevations is low, a weak correlation of high errors with high terrace elevations can be observed.

4.3.   Coastal uplift-rate estimates

We calculated uplift rates from 1953 terrace-elevation measurements of MIS-5e (1843) and MIS-5c (110) along the WSAC with a median uplift rate of approximately 0.22 m/ka (Fig. 11). As with the distribution of terrace elevations, we similarly observed several small-scale and large-scale, high-amplitude changes in uplift rate along the coast. The most pronounced long-wavelength highs (≥ 1° latitude) in uplift rate are located on the Manta Peninsula (0.79 m/ka), in the San Juan de Marcona area (0.85 m/ka), and on the Arauco Peninsula (1.62 m/ka). Medium-wavelength structures include the Mejillones Peninsula (0.47 m/ka) and Topocalma (1.43 m/ka), while shorter wavelength structures that are characterized by exceptionally high uplift rates seem to be limited to the central Chilean part of the coastline, especially between 31.5° and 40°S. The most striking example includes Carranza with an uplift rate of up to 0.87 m/ka since the formation of the oldest MIS-5 terrace levels. Lower, but still quite high, uplift rates were calculated for areas north of Los Vilos (0.46 m/ka), near Valparaíso (0.49 m/ka), and near Valdivia (0.59 m/ka). The lowest uplift rates along the South American margin occur at Penco immediately north of Concepción (0.03 m/ka), south of Chiclayo in northern Peru (0.07 m/ka), and on the southern Santa Elena Peninsula in Ecuador (0.07 m/ka).

5. Discussion

5.1. Advantages and limitations of the database of last interglacial marine terrace elevations along the WSAC

In this study we generated a systematic database of last interglacial marine terrace elevations with unprecedented resolution based on an almost continuous mapping of ~2,000 measurements along 5,000 km of the WSAC. This opens up several possibilities for future applications in which this database can be used; for example, marine terraces are excellent strain markers that can be used in studies on deformation processes at regional scale, and thus the synthesis allows comparisons between deformation rates at different temporal scales in different sectors of the margin or analyses linking specific climate-driven and tectonic coastal processes, and landscape evolution. However, there are a number of limitations and potential uncertainties that can limit the use of this database in such studies without taking several caveats into consideration.

One of the most critical limitations of using the database is associated with the referencing points used to tie our marine terrace measurements, which are in turn based on the results and chronological constraints provided by previous studies. The referencing points are heterogeneously distributed along the WSAC, resulting in some cases of up to 600 km distance to the nearest constrained point, such as in Central Peru [e.g. Pe2]. This may have a strong influence on the confidence in the measurement of the marine terrace elevation at these sites. In addition, the geochronological control of some of the referencing points may be based on dating methods with pronounced uncertainties (e.g., amino acid racemization, electron spin resonance, terrestrial cosmogenic radionuclides), which may result in equivocal interpretations and chronologies of marine terrace levels. In order to address these potential factors of uncertainty we defined a quality rating (see section 3.1.), which allows classifying our mapping results based on their confidence and reliability. Therefore, by considering measurements above a defined quality it is possible to increase the level of confidence for future studies using this database; however, this might result in a decrease of the number of measurements available for analysis and comparison.

5.2. Tectonic and climatic controls on the elevation and morphology of marine terraces along the WSAC

In this section we provide a brief synthesis of our data set and its implications for coastal processes and overall landscape evolution influenced by a combination of tectonic and climatic forcing factors. This synthesis emphasizes the significance of our comprehensive data set for a variety of coastal research problems that were briefly introduced in section 5.1. Our detailed measurements of marine terraces along the WSAC reveal variable elevations and a heterogeneous distribution of uplift rates associated with patterns of short-, medium-, and long-wavelengths. In addition, we observe different degrees of development of marine terraces along the margin expressed in variable shoreline-angle density. There are several possible causes for this variability, which we explore by comparing terrace-elevation patterns with different climatic and tectonic parameters.

5.2.1. Tectonic controls on coastal uplift rates

The spatial distribution of the MIS-5 marine terrace elevations along the convergent South American margin has revealed several high-amplitude and long-wavelength changes with respect to tectonically controlled topography. Long-wavelength patterns in terrace elevation ($\sim 10^2$ km) are observed at the Manta Peninsula in Ecuador, central Peru between Chiclayo and Lima, San Juan de Marcona (Peru), and on the Arauco Peninsula in Chile, while medium-wavelength structures occur at Mejillones Peninsula and Topocalma (Chile). Instead, short-wavelength patterns in MIS-5 terrace elevations are observed, for instance, near Los Vilos, Valparaíso, and Carranza in Chile.

The subduction of bathymetric anomalies has been shown to exert a substantial influence on upper-plate deformation (Fryer and Smoot, 1985; Taylor et al., 1987; Macharé and Ortlieb, 1992; Cloos and Shreve, 1996; Gardner et al., 2013; Wang and Bilek, 2014; Ruh et al., 2016), resulting in temporally and spatially variable fault activity, kinematics, and deformation rates (Mann et al., 1998; Saillard et al., 2011; Morgan and Bangs, 2017; Melnick et al., 2019). When comparing the uplift pattern of MIS-5 marine terraces and the bathymetry of the oceanic plate, we observe that the two long-wavelength structures in this area, on the Manta Peninsula and at San Juan de Marcona, both coincide with the location of the subducting Nazca and Carnegie ridges, respectively (Fig. 11A and B); this was also previously observed by other authors (Macharé and Ortlieb, 1992; Gutscher et al., 1999; Pedoja et al., 2006a; Saillard et al., 2011). In summary, long-wavelength structures in coastal areas of the upper plate may be associated with deep-seated processes (Melosh and Raefsky, 1980; Watts and Daly, 1981) possibly related to changes in the mechanical behavior of the plate interface. In this context it is interesting that the high uplift rates on the Arauco Peninsula do not correlate with bathymetric anomalies, which may suggest a different deformation mechanism. The scarcity of crustal faults described in the Arauco area rather suggests that shallow structures associated with crustal bending and splay-faults occasionally breaching through the upper crust (Melnick et al., 2012; Jara-Muñoz et al., 2015; Jara-Muñoz et al., 2017; Melnick et al., 2019) may cause long-wavelength warping and uplift there (Fig. 11A).

In contrast, small-scale bathymetric anomalies correlate in part with the presence of crustal faults perpendicular to the coastal margin near, for instance, the Juan Fernandez, Taltal, and Copiapó ridges (Fig. 11B); this results in short-wavelength structures and a more localized altitudinal differentiation of uplifted terraces. This emphasizes also the importance of last interglacial marine terraces as strain markers with respect to currently active faults, which might be compared in the future with short-term deformation estimates from GPS or the earthquake catalog. In summary, short-wavelength structures in the coastal realms of western South America may be associated with faults that root at shallow depths within the continental crust (Jara-Muñoz et al., 2015; Jara-Muñoz et al., 2017; Melnick et al., 2019).

The thickness of sediment in the trench is an additional controlling factor on forearc architecture that may determine which areas of the continental margin are subjected to subduction erosion or accretion (Hilde, 1983; Cloos and Shreve, 1988; Menant et al., 2020). Our data shows that the accretionary part of the WSAC (south of the intersection with the Juan Fernandez Ridge at 32.9°S) displays faster median uplift rates of 0.26 m/ka than in the rest of the WSAC (Fig. 11B and C). However, no clear correlation is observed between trench fill, uplift rates, and the different structural patterns in the erosive part of the margin. On the other hand, we observe lower uplift rates for greater distances from the trench at the Arica bend, in central Peru, and in the Gulf of Guayaquil, while higher uplift rates occur in areas closer to the trench, such as near the Nazca and Carnegie ridges and the Mejillones Peninsula.

5.2.2. Climatic controls on the formation and preservation of last interglacial marine terraces

The latitudinal climate differences that characterize the western margin of South America may also control coastal morphology and the generation and preservation of marine terraces (Martinod et al., 2016b). In order to evaluate the influence of climate in the generation and/or degradation of marine terraces, we compared the number of marine terrace measurements, which is a proxy for the degree of marine terrace preservation, and climatically controlled parameters such as wave height, tidal range, coastline orientation, and the amount of precipitation.

The maximum wave height along the WSAC decreases northward from ~8 to ~2 m (see section 3.3, Fig. 11D). Similarly, the tidal range decreases progressively northward from 2 to 1 m between Valdivia and San Juan de Marcona, followed by a rapid increase to 4 m between San Juan de Marcona and the Manta Peninsula. We observe an apparent correlation between the number of measurements and the tidal range in the north, between Illescas and Manta (Fig. 11F). Likewise, the increasing trend in the number of measurements southward matches with the increase in wave height (Fig. 11D). An increase of wave height and tidal range may lead to enhanced erosion and morphologically well-expressed marine terraces (Anderson et al., 1999; Trenhaile, 2002), which is consequently reflected in a higher number of measurements that can be carried out. Furthermore, we observe low values for the reference water level (< 0.7 m) resulting from tide and wave-height estimations in IMCalc (Lorscheid and Rovere, 2019), which are used to correct our shoreline-angle measurements in the WALIS database (see section 3.3.).

The control of wave-erosion processes on the morphological expression of marine terraces may be counteracted by erosional processes such as river incision. We note that the high number of preserved marine terraces between Mejillones and Valparaíso decreases southward, which coincides with a sharp increase in mean annual precipitation from 10 to 1000 mm/yr (Fig. 11E and F) and fluvial dissection. However, in the area with a high number of measurements between the Illescas Peninsula and Manta we observe an opposite correlation: higher rainfall associated with an increase of marine terrace preservation (Fig. 11E). This suggests that the interplay between marine terrace generation and degradation processes apparently buffer each other, resulting in different responses under different climatic conditions and coastal settings.

The higher greater number of marine terraces between Mejillones and Valparaíso and north of Illescas corresponds with a SSW-NNE orientation of the coastline (azimuth between 200 and 220°). In contrast, NW-SE to N-S oriented coastlines (azimuth between 125 and 180°), such as between the Arica and Huancabamba bends, correlate with a lower number of marine terrace measurements (Fig. 11E and F). This observation appears, however, implausible considering that NW-SE oriented coastlines may be exposed more directly to the erosive effect of storm waves associated with winds approaching from the south. We interpret the orientation of the coastline therefore to be of secondary importance at regional scale for the formation of marine terraces compared to other parameters, such as wave height, tidal range, or rainfall.
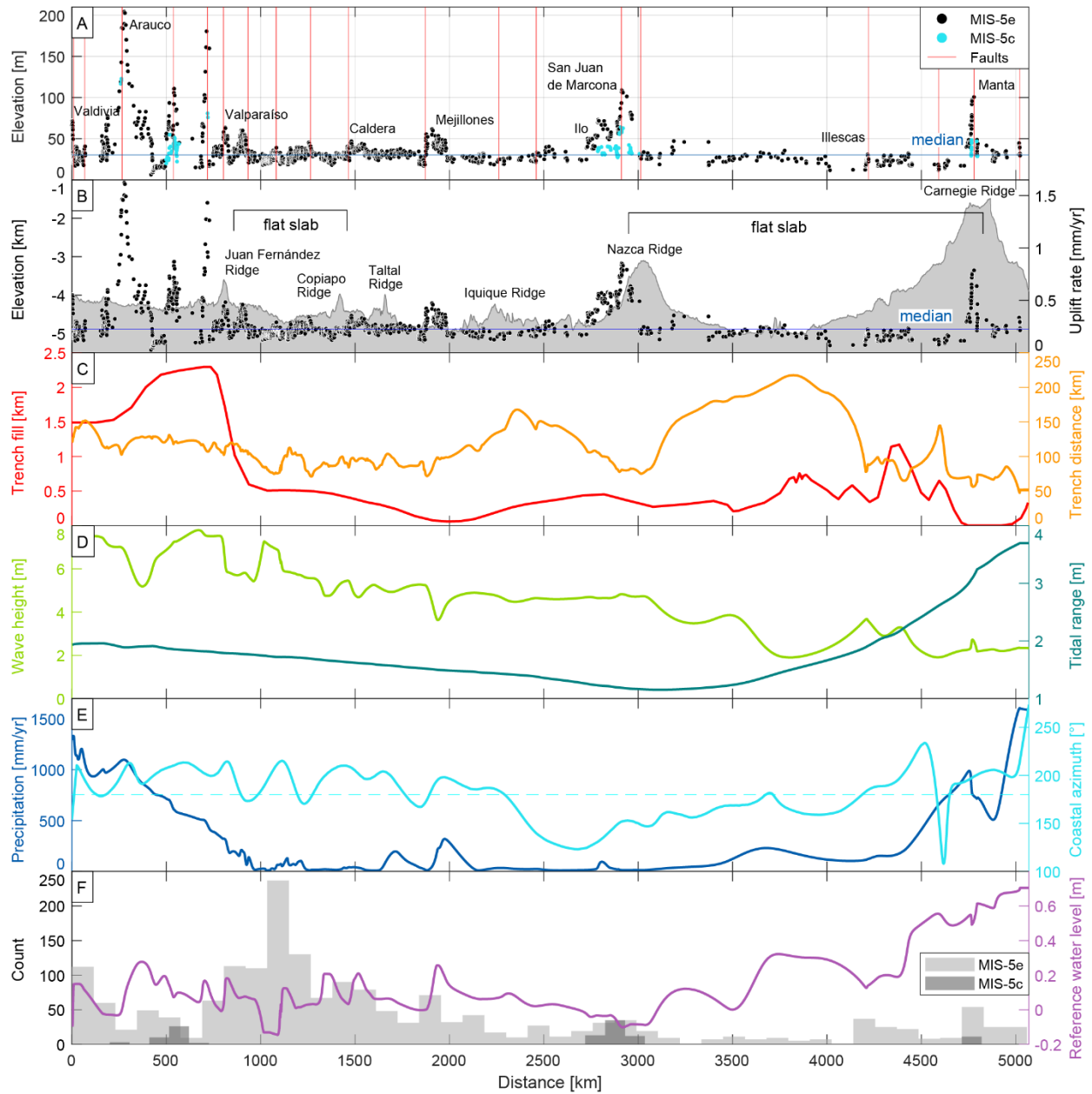
Figure 11. Terrace-elevation and uplift-rate estimates plotted in comparison with various parameters (i.e., bathymetry, trench fill, trench distance, wave height, tidal range, precipitation, and coastal azimuth) that might influence the disparate characteristics of the marine terrace distribution revealed by our data set. We projected these parameters, elevations, and uplift rates with respect to a S-N-oriented polyline that represents the trench. **(A)** Terrace-elevation measurements and most important crustal faults (Veloza et al., 2012; Melnick et al., 2020). This shows the range of altitudes in different regions along the coast and possible relationships between terrace elevation and crustal faulting. The blue horizontal line indicates the median elevation (30.1 m). **(B)** Coastal uplift rates and mean bathymetry (GEBCO Bathymetric Compilation Group, 2020) of a 150-km-swath west of the trench. The blue horizontal line indicates the median uplift rate (0.22 mm/a). **(C)** Sediment thickness of trench-fill deposits (red) (Bangs and Cande, 1997) and the distance of the trench from our terrace measurements (orange). Flat-slab segments of the subducting Nazca plate are indicated for central Chile and Peru. **(D)** Maximum wave heights along the WSAC (light green) and the tidal range (dark green) between highest and lowest astronomical tides (Lorscheid and Rovere, 2019). **(E)** Precipitation (blue) along the WSAC (Ceccherini et al., 2015) and azimuthal orientation of the coastline (cyan). **(F)** Histogram of terrace-elevation measurements along the WSAC.

6.   Conclusions

We measured 1,953 shoreline-angle elevations as proxies for paleo-sea levels of the MIS-5e and 5c terraces along ~5,000 km of the WSAC between Ecuador and Southern Chile. Our measurements are based on a systematic methodology and the resulting data have been standardized within the framework of the WALIS database. Our mapping was tied using referencing points based on previously published terrace-elevation estimates and age constraints that are summarized in the compilation of Pedoja et al. (2011). The limitations of this database are associated with the temporal accuracy and spatial distribution of the referencing points, which we attempt to consider by providing a quality-rating value to each measurement. The marine terrace elevations display a median value of 30.1 m for the MIS-5e level and a median uplift rate of 0.22 m/ka for MIS-5e and 5c. The lowest terrace elevations and uplift rates along the entire WSAC occur immediately north of Concepción in Chile (6 m, 0.03 m/ka), south of Chiclayo in northern Peru, and on the Santa Elena Peninsula in Ecuador (both 12 m, 0.07 m/ka). The regions with exceptionally high marine terrace elevations ($\geq$ 100 m) comprise the Manta Peninsula in Ecuador, the San Juan de Marcona area in south-central Peru, and three regions in south-central Chile (Topocalma, Carranza, and Arauco).

The pattern of terrace elevations displays short-, medium- and long-wavelength structures controlled by a combination of various mechanisms. Long-wavelength structures may be controlled by deep-seated processes at the plate interface, such as the subduction of major bathymetric anomalies (e.g. Manta Peninsula and San Juan de Marcona region). In contrast, short- and medium-wavelength deformation patterns may be controlled by crustal faults rooted within the upper plate (e.g., between Mejillones and Valparaíso).

Latitudinal climate characteristics along the WSAC may influence the generation and preservation of marine terraces. An increase in wave height and tidal range generally results in enhanced erosion and morphologically well-expressed, sharply defined marine terraces, which correlates with the southward increase in the number of our marine terrace measurements. Conversely, river incision and lateral scouring in areas with high precipitation may degrade marine terraces, thus decreasing the number of potential marine terrace measurements, such as observed south of Valparaíso.

Data availability. The South American database of last interglacial shoreline-angle elevations is available online at http://doi.org/10.5281/zenodo.4309748 (Freisleben et al., 2020). The description of the WALIS-database fields can be found at https://doi.org/10.5281/zenodo.3961543 (Rovere et al., 2020).

Author contributions. The main compilers of the database were R.F., J.M.M., and J.J. The paper was written by R.F. with significant input from J.J., D.M., M.S. regarding interpretation and further improvements of graphical data representation.

Acknowledgments. We thank Alessio Rovere for his assistance with the WALIS database. The WALIS database was developed by the ERC Starting Grant "Warmcoasts" (ERC-StG-802414) and PALSEA. PALSEA is a working group of the International Union for Quaternary Sciences (INQUA) and Past Global Changes (PAGES), which in turn received support from the Swiss Academy of Sciences and the Chinese Academy of Sciences. The structure of the database was designed by A. Rovere, D. Ryan, T. Lorscheid, A. Dutton, P. Chutcharavan, D. Brill, N. Jankowski, D. Mueller, M. Bartz, E.J. Gowan and K. Cohen. This study was supported by the Millennium Scientific Initiative of the Chilean government through grant NC160025 "Millennium Nucleus CYCLO The Seismic Cycle Along Subduction Zones", Chilean National Fund for Development of Science and Technology (FONDECYT) grants 1181479 and 1190258, the ANID PIA Anillo ACT192169. R.F. was supported by a research grant of Deutsche

837 Forschungsgemeinschaft to M.S. (DFG STR373/41-1). Constructive reviews by V. Regard and P.M. Figueiredo
838 helped to improve the paper.

839

7.   References

841 Anderson, R.S., Densmore, A.L., Ellis, M.A., 1999. The generation and degradation of marine terraces. Basin
842   Research 11(1), 7–19. doi:10.1046/j.1365-2117.1999.00085.x.

843 Angermann, D., Klotz, J., Reigber, C., 1999. Space-geodetic estimation of the Nazca-South America Euler vector.
844   Earth and Planetary Science Letters 171(3), 329–334. doi:10.1016/S0012-821X(99)00173-9.

845 Baker, A., Allmendinger, R.W., Owen, L.A., Rech, J.A., 2013. Permanent deformation caused by subduction
846   earthquakes in northern Chile. Nature Geoscience 6(6), 492–496. doi:10.1038/ngeo1789.

847 Bangs, N.L., Cande, S.C., 1997. Episodic development of a convergent margin inferred from structures and
848   processes along the southern Chile margin. Tectonics 16(3), 489–503.

849 Barazangi, M., Isacks, B.L., 1976. Spatial distribution of earthquakes and subduction of the Nazca plate beneath
850   South America. Geology 4(11), 686. doi:10.1130/0091-7613(1976)4<686:SDOEAS>2.0.CO;2.

851 Beck, S., Barrientos, S., Kausel, E., Reyes, M., 1998. Source characteristics of historic earthquakes along the central
852   Chile subduction zone. Journal of South American Earth Sciences 11(2), 115–129. doi:10.1016/S0895-
853   9811(98)00005-4.

854 Bendix, J., Rollenbeck, R., Reudenbach, C., 2006. Diurnal patterns of rainfall in a tropical Andean valley of
855   southern Ecuador as seen by a vertically pointing K-band Doppler radar. International Journal of Climatology
856   26(6), 829–846. doi:10.1002/joc.1267.

857 Bernhardt, A., Hebbeln, D., Regenberg, M., Lückge, A., Strecker, M.R., 2016. Shelfal sediment transport by an
858   undercurrent forces turbidity-current activity during high sea level along the Chile continental margin. Geology
859   44(4), 295–298. doi:10.1130/G37594.1.

860 Bernhardt, A., Schwanghart, W., Hebbeln, D., Stuut, J.-B.W., Strecker, M.R., 2017. Immediate propagation of
861   deglacial environmental change to deep-marine turbidite systems along the Chile convergent margin. Earth and
862   Planetary Science Letters 473, 190–204. doi:10.1016/j.epsl.2017.05.017.

863 Bilek, S.L., 2010. Invited review paper: Seismicity along the South American subduction zone: Review of large
864   earthquakes, tsunamis, and subduction zone complexity. Tectonophysics 495(1-2), 2–14.
865   doi:10.1016/j.tecto.2009.02.037.

866 Bilek, S.L., Schwartz, S.Y., DeShon, H.R., 2003. Control of seafloor roughness on earthquake rupture behavior.
867   Tectonics 31(5), 455. doi:10.1130/0091-7613(2003)031<0455:COSROE>2.0.CO;2.

868   Binnie, A., Dunai, T.J., Binnie, S.A., Victor, P., González, G., Bolten, A., 2016. Accelerated late quaternary uplift
869   revealed by 10Be exposure dating of marine terraces, Mejillones Peninsula, northern Chile. Quaternary
870   Geochronology 36, 12–27. doi:10.1016/j.quageo.2016.06.005.

871   Bookhagen, B., Strecker, M.R., 2008. Orographic barriers, high-resolution TRMM rainfall, and relief variations
872   along the eastern Andes. Geophysical Research Letters 35(6), 139. doi:10.1029/2007GL032011.

873   Cahill, T., Isacks, B.L., 1992. Seismicity and shape of the subducted Nazca Plate. Journal of Geophysical Research
874   97(B12), 17503. doi:10.1029/92JB00493.

875   Ceccherini, G., Ameztoy, I., Hernández, C., Moreno, C., 2015. High-Resolution Precipitation Datasets in South
876   America and West Africa based on Satellite-Derived Rainfall, Enhanced Vegetation Index and Digital Elevation
877   Model. Remote Sensing 7(5), 6454–6488. doi:10.3390/rs70506454.

878   Cembrano, J., Lavenu, A., Yañez, G., Riquelme, R., García, M., González, G., Hérail, G., 2007. Neotectonics. In:
879   Moreno, T., Gibbons, W. (Eds.), The geology of Chile. Geological Society, London, pp. 231–261.

880   Clift, P., Vannucchi, P., 2004. Controls on tectonic accretion versus erosion in subduction zones: Implications for
881   the origin and recycling of the continental crust. Reviews of Geophysics 42(2), 19. doi:10.1029/2003RG000127.

882   Clift, P.D., Hartley, A.J., 2007. Slow rates of subduction erosion and coastal underplating along the Andean margin
883   of Chile and Peru. Geology 35(6), 503. doi:10.1130/G23584A.1.

884   Cloos, M., Shreve, R.L., 1988. Subduction-channel model of prism accretion, melange formation, sediment
885   subduction, and subduction erosion at convergent plate margins: 1. Background and description. Pure and
886   Applied Geophysics 128(3-4), 455–500. doi:10.1007/BF00874548.

887   Cloos, M., Shreve, R.L., 1996. Shear-zone thickness and the seismicity of Chilean- and Marianas-type subduction
888   zones. Geology 24(2), 107. doi:10.1130/0091-7613(1996)024<0107:SZTATS>2.3.CO;2.

889   Collot, J.-Y., Charvis, P., Gutscher, M.-A., Operto, S., 2002. Exploring the Ecuador-Colombia Active Margin and
890   Interplate Seismogenic Zone. Eos, Transactions, American Geophysical Union 83(17), 185.
891   doi:10.1029/2002EO000120.

892   Collot, J.-Y., Sanclemente, E., Nocquet, J.-M., Leprêtre, A., Ribodetti, A., Jarrin, P., Chlieh, M., Graindorge, D.,
893   Charvis, P., 2017. Subducted oceanic relief locks the shallow megathrust in central Ecuador. Journal of
894   Geophysical Research: Solid Earth 122(5), 3286–3305. doi:10.1002/2016JB013849.

895   Costa, C., Alvarado, A., Audemard, F., Audin, L., Benavente, C., Bezerra, F.H., Cembrano, J., González, G., López,
896   M., Minaya, E., Santibañez, I., Garcia, J., Arcila, M., Pagani, M., Pérez, I., Delgado, F., Paolini, M., Garro, H.,
897   2020. Hazardous faults of South America; compilation and overview. Journal of South American Earth Sciences
898   104(1), 102837. doi:10.1016/j.jsames.2020.102837.

899   Costa, C., Machette, M.N., Dart, R.L., Bastias, H.E., Paredes, J.D., Perucca, L.P., Tello, G.E., Haller, K.M., 2000.
900   Map and database of Quaternary faults and folds in Argentina. Open-File Report. US Geological Survey.
901   http://dx.doi.org/10.3133/ofr00108.

902   Coudurier-Curveur, A., Lacassin, R., Armijo, R., 2015. Andean growth and monsoon winds drive landscape
903   evolution at SW margin of South America. Earth and Planetary Science Letters 414, 87–99.
904   doi:10.1016/j.epsl.2014.12.047.

905   Creveling, J.R., Mitrovica, J.X., Clark, P.U., Waelbroeck, C., Pico, T., 2017. Predicted bounds on peak global mean
906   sea level during marine isotope stages 5a and 5c. Quaternary Science Reviews 163(6), 193–208.
907   doi:10.1016/j.quascirev.2017.03.003.

908   DeMets, C., Gordon, R.G., Argus, D.F., 2010. Geologically current plate motions. Geophysical Journal International
909   181(1), 1–80. doi:10.1111/j.1365-246X.2009.04491.x.

910   Espurt, N., Funiciello, F., Martinod, J., Guillaume, B., Regard, V., Faccenna, C., Brusset, S., 2008. Flat subduction
911   dynamics and deformation of the South American plate: Insights from analog modeling. Tectonics 27(3), n/a-
912   n/a. doi:10.1029/2007TC002175.

913   Freisleben, R., Jara-Muñoz, J., Melnick, D., Martínez, J.M., Strecker, M., 2020. Marine terraces of the last
914   interglacial period along the Pacific coast of South America (1°N-40°S). Zenodo.
915   doi:10.5281/ZENODO.4309748.

916   Fryer, P., Smoot, N.C., 1985. Processes of seamount subduction in the Mariana and Izu-Bonin trenches. Marine
917   Geology 64(1-2), 77–90. doi:10.1016/0025-3227(85)90161-6.

918   Fuenzalida, H., Cooke, R., Paskoff, R., Segerstrom, K., Weischet, W., 1965. High Stands of Quaternary Sea Level
919   Along the Chilean Coast. Geological Society of America Special Papers 84, 473–496.

920   Gallen, S.F., Wegmann, K.W., Bohnenstiehl, D.R., Pazzaglia, F.J., Brandon, M.T., Fassoulas, C., 2014. Active
921   simultaneous uplift and margin-normal extension in a forearc high, Crete, Greece. Earth and Planetary Science
922   Letters 398, 11–24. doi:10.1016/j.epsl.2014.04.038.

923   Gardner, T.W., Fisher, D.M., Morell, K.D., Cupper, M.L., 2013. Upper-plate deformation in response to flat slab
924   subduction inboard of the aseismic Cocos Ridge, Osa Peninsula, Costa Rica. Lithosphere 5(3), 247–264.
925   doi:10.1130/L251.1.

926   Garreaud, R.D., 2009. The Andes climate and weather. Advances in Geosciences 22, 3–11. doi:10.5194/adgeo-22-3-
927   2009.

928   GEBCO Bathymetric Compilation Group, 2020. The GEBCO_2020 Grid - a continuous terrain model of the global
929   oceans and land. British Oceanographic Data Centre, National Oceanography Centre, NERC, UK.

930   Geersen, J., Ranero, C.R., Barckhausen, U., Reichert, C., 2015. Subducting seamounts control interplate coupling
931   and seismic rupture in the 2014 Iquique earthquake area. Nature communications 6, 8267.
932   doi:10.1038/ncomms9267.

933   German Aerospace Center (DLR), 2018. TanDEM-X - Digital Elevation Model (DEM) - Global, 12m.

934   González, G., Carrizo, D., 2003. Segmentación, cinemática y cronología relativa de la deformación tardía de la Falla
935   Salar del Carmen, Sistema de Fallas de Atacama, (23°40'S), norte de Chile. Revista Geológica de Chile 30(2).
936   doi:10.4067/S0716-02082003000200005.

937   Goy, J.L., Macharé, J., Ortlieb, L., Zazo, C., 1992. Quaternary shorelines in Southern Peru a record of global sea-
938   level fluctuations and tectonic uplift in Chala Bay. Quaternary International 15-16, 99–112.

939   Gutscher, M.-A., Malavieille, J., Lallemand, S., Collot, J.-Y., 1999. Tectonic segmentation of the North Andean
940   margin: impact of the Carnegie Ridge collision. Earth and Planetary Science Letters 168(3-4), 255–270.
941   doi:10.1016/S0012-821X(99)00060-6.

942   Gutscher, M.-A., Spakman, W., Bijwaard, H., Engdahl, E.R., 2000. Geodynamics of flat subduction: Seismicity and
943   tomographic constraints from the Andean margin. Tectonics 19(5), 814–833. doi:10.1029/1999TC001152.

944   Hampel, A., 2002. The migration history of the Nazca Ridge along the Peruvian active margin: a re-evaluation.
945   Earth and Planetary Science Letters 203(2), 665–679. doi:10.1016/S0012-821X(02)00859-2.

946   Hayes, G.P., Moore, G.L., Portner, D.E., Hearne, M., Flamme, H., Furtney, M., Smoczyk, G.M., 2018. Slab2, a
947   comprehensive subduction zone geometry model. Science (New York, N.Y.) 362(6410), 58–61.
948   doi:10.1126/science.aat4723.

949   Hearty, P.J., Hollin, J.T., Neumann, A.C., O'Leary, M.J., McCulloch, M., 2007. Global sea-level fluctuations during
950   the Last Interglaciation (MIS 5e). Quaternary Science Reviews 26(17-18), 2090–2112.
951   doi:10.1016/j.quascirev.2007.06.019.

952   Hilde, T.W.C., 1983. Sediment subduction versus accretion around the pacific. Tectonophysics 99(2-4), 381–397.
953   doi:10.1016/0040-1951(83)90114-2.

954   Houston, J., Hartley, A.J., 2003. The central Andean west-slope rainshadow and its potential contribution to the
955   origin of hyper-aridity in the Atacama Desert. International Journal of Climatology 23(12), 1453–1464.
956   doi:10.1002/joc.938.

957   Hsu, J.T., 1992. Quaternary uplift of the Peruvian coast related to the subduction of the Nazca Ridge: 13.5 to 15.6
958   degrees south latitude. Quaternary International 15-16, 87–97. doi:10.1016/1040-6182(92)90038-4.

959   Hsu, J.T., Leonard, E.M., Wehmiller, J.F., 1989. Aminostratigraphy of Peruvian and Chilean Quaternary marine
960   terraces. Quaternary Science Reviews 8(3), 255–262. doi:10.1016/0277-3791(89)90040-1.

961   Huene, R. von, Pecher, I.A., Gutscher, M.-A., 1996. Development of the accretionary prism along Peru and material
962   flux after subduction of Nazca Ridge. Tectonics 15(1), 19–33. doi:10.1029/95TC02618.

963   Jaillard, E., Hérail, G., Monfret, T., Díaz-Martínez, E., Baby, P., Lavenu, A., Dumont, J.F., 2000. Tectonic evolution
964   of the Andes of Ecuador, Peru, Bolivia, and northernmost Chile. In: Cordani, U.G., Milani, E.J., Thomaz, F.A.,
965   Campos, D.A. (Eds.), Tectonic evolution of South America. Sociedad Brasileira de Geologia, Rio de Janeiro,
966   pp. 481–559.

967   Jara-Muñoz, J., Melnick, D., Brill, D., Strecker, M.R., 2015. Segmentation of the 2010 Maule Chile earthquake
968   rupture from a joint analysis of uplifted marine terraces and seismic-cycle deformation patterns. Quaternary
969   Science Reviews 113, 171–192. doi:10.1016/j.quascirev.2015.01.005.

970   Jara-Muñoz, J., Melnick, D., Socquet, A., Cortés-Aranda, J., Strecker, M.R., 2018. Slip rate and earthquake
971   recurrence of the Pichilemu Fault. Congreso Geológico Chileno, 15th.

972   Jara-Muñoz, J., Melnick, D., Strecker, M.R., 2016. TerraceM: A MATLAB® tool to analyze marine and lacustrine
973   terraces using high-resolution topography. Geosphere 12(1), 176–195. doi:10.1130/GES01208.1.

974   Jara-Muñoz, J., Melnick, D., Zambrano, P., Rietbrock, A., González, J., Argandoña, B., Strecker, M.R., 2017.
975   Quantifying offshore fore-arc deformation and splay-fault slip using drowned Pleistocene shorelines, Arauco
976   Bay, Chile. Journal of Geophysical Research: Solid Earth 122(6), 4529–4558. doi:10.1002/2016JB013339.

977   Jordan, T.E., Isacks, B.L., Allmendinger, R.W., Brewer, J.A.O.N., Ramos, V.A., Ando, C.J., 1983. Andean tectonics
978   related to geometry of subducted Nazca plate. Geological Society of America Bulletin 94(3), 341.
979   doi:10.1130/0016-7606(1983)94<341:ATRTGO>2.0.CO;2.

980   Kay, S.M., Maksaev, V., Moscoso, R., Mpodozis, C., Nasi, C., 1987. Probing the evolving Andean Lithosphere:
981   Mid-Late Tertiary magmatism in Chile (29°–30°30′S) over the modern zone of subhorizontal subduction.
982   Journal of Geophysical Research 92(B7), 6173. doi:10.1029/JB092iB07p06173.

983   Lajoie, K.R., 1986. Coastal tectonics. In: Wallace, R.E. (Ed.), Active tectonics. National Academics Press,
984   Washington D.C., pp. 95–124.

985   Lamb, S., Davis, P., 2003. Cenozoic climate change as a possible cause for the rise of the Andes. Nature 425(6960),
986   792–797. doi:10.1038/nature02049.

987   Lohrmann, J., Kukowski, N., Adam, J., Oncken, O., 2003. The impact of analogue material properties on the
988   geometry, kinematics, and dynamics of convergent sand wedges. Journal of Structural Geology 25(10), 1691–
989   1711. doi:10.1016/S0191-8141(03)00005-1.

990   Lorscheid, T., Rovere, A., 2019. The indicative meaning calculator – quantification of paleo sea-level relationships
991   by using global wave and tide datasets. Open Geospatial Data, Software and Standards 4(1), 591.
992   doi:10.1186/s40965-019-0069-8.

993 Macharé, J., Ortlieb, L., 1992. Plio-Quaternary vertical motions and the subduction of the Nazca Ridge, central coast
994   of Peru. Tectonophysics 205(1-3), 97–108. doi:10.1016/0040-1951(92)90420-B.

995 Maldonado, V., Contreras, M., Melnick, D., 2021. A comprehensive database of active and potentially-active
996   continental faults in Chile at 1:25,000 scale. Scientific data 8(1), 20. doi:10.1038/s41597-021-00802-4.

997 Manea, V.C., Pérez-Gussinyé, M., Manea, M., 2012. Chilean flat slab subduction controlled by overriding plate
998   thickness and trench rollback. Geology 40(1), 35–38. doi:10.1130/G32543.1.

999 Mann, P., Taylor, F.W., Lagoe, M.B., Quarles, A., Burr, G., 1998. Accelerating late Quaternary uplift of the New
1000   Georgia Island Group (Solomon island arc) in response to subduction of the recently active Woodlark spreading
1001   center and Coleman seamount. Tectonophysics 295(3-4), 259–306. doi:10.1016/S0040-1951(98)00129-2.

1002 Marcaillou, B., Collot, J.-Y., Ribodetti, A., d'Acremont, E., Mahamat, A.-A., Alvarado, A., 2016. Seamount
1003   subduction at the North-Ecuadorian convergent margin: Effects on structures, inter-seismic coupling and
1004   seismogenesis. Earth and Planetary Science Letters 433, 146–158. doi:10.1016/j.epsl.2015.10.043.

1005 Martinod, J., Regard, V., Letourmy, Y., Henry, H., Hassani, R., Baratchart, S., Carretier, S., 2016a. How do
1006   subduction processes contribute to forearc Andean uplift? Insights from numerical models. Journal of
1007   Geodynamics 96, 6–18. doi:10.1016/j.jog.2015.04.001.

1008 Martinod, J., Regard, V., Riquelme, R., Aguilar, G., Guillaume, B., Carretier, S., Cortés-Aranda, J., Leanni, L.,
1009   Hérail, G., 2016b. Pleistocene uplift, climate and morphological segmentation of the Northern Chile coasts
1010   (24°S–32°S): Insights from cosmogenic 10Be dating of paleoshorelines. Geomorphology 274, 78–91.
1011   doi:10.1016/j.geomorph.2016.09.010.

1012 Melet, A., Teatini, P., Le Cozannet, G., Jamet, C., Conversi, A., Benveniste, J., Almar, R., 2020. Earth Observations
1013   for Monitoring Marine Coastal Hazards and Their Drivers. Surveys in Geophysics 41(6), 1489–1534.
1014   doi:10.1007/s10712-020-09594-5.

1015 Melnick, D., 2016. Rise of the central Andean coast by earthquakes straddling the Moho. Nature Geoscience 9(5),
1016   401–407. doi:10.1038/ngeo2683.

1017 Melnick, D., Bookhagen, B., Echtler, H.P., Strecker, M.R., 2006. Coastal deformation and great subduction
1018   earthquakes, Isla Santa Maria, Chile (37°S). Geological Society of America Bulletin 118(11-12), 1463–1480.
1019   doi:10.1130/B25865.1.

1020 Melnick, D., Bookhagen, B., Strecker, M.R., Echtler, H.P., 2009. Segmentation of megathrust rupture zones from
1021   fore-arc deformation patterns over hundreds to millions of years, Arauco peninsula, Chile. Journal of
1022   Geophysical Research: Solid Earth 114(B1), 6140. doi:10.1029/2008JB005788.

1023 Melnick, D., Hillemann, C., Jara-Muñoz, J., Garrett, E., Cortés-Aranda, J., Molina, D., Tassara, A., Strecker, M.R.,
1024   2019. Hidden Holocene slip along the coastal El Yolki Fault in Central Chile and its possible link with

1025   megathrust earthquakes. Journal of Geophysical Research: Solid Earth 124(7), 7280–7302.
1026   doi:10.1029/2018JB017188.

1027   Melnick, D., Maldonado, V., Contreras, M., 2020. Database of active and potentially-active continental faults in
1028   Chile at 1:25,000 scale. PANGAEA - Data Publisher for Earth & Environmental Science.
1029   doi:10.1594/PANGAEA.922241.

1030   Melosh, H.J., Raefsky, A., 1980. The dynamical origin of subduction zone topography. Geophysical Journal
1031   International 60(3), 333–354. doi:10.1111/j.1365-246X.1980.tb04812.x.

1032   Menant, A., Angiboust, S., Gerya, T., Lacassin, R., Simoes, M., Grandin, R., 2020. Transient stripping of
1033   subducting slabs controls periodic forearc uplift. Nature communications 11(1), 1823. doi:10.1038/s41467-020-
1034   15580-7.

1035   Morgan, J.K., Bangs, N.L., 2017. Recognizing seamount-forearc collisions at accretionary margins: Insights from
1036   discrete numerical simulations. Geology 45(7), 635–638. doi:10.1130/G38923.1.

1037   Müller, R.D., Sdrolias, M., Gaina, C., Roest, W.R., 2008. Age, spreading rates, and spreading asymmetry of the
1038   world's ocean crust. Geochemistry, Geophysics, Geosystems 9(4). doi:10.1029/2007GC001743.

1039   Naranjo, J.A., 1987. Interpretacion de la actividad cenozoica superior a lo largo de la Zona de Falla Atacama, Norte
1040   de Chile. Revista Geológica de Chile(31), 43–55.

1041   Ortlieb, L., Macharé, J., 1990. Geochronologia y morfoestratigrafia de terrazas marinas del Pleistoceno superior: El
1042   caso de San Juan-Marcona, Peru. Boletín de la Sociedad Geológica del Perú 81, 87–106.

1043   Ortlieb, L., Zazo, C., Goy, J., Hillaire-Marcel, C., Ghaleb, B., Cournoyer, L., 1996a. Coastal deformation and sea-
1044   level changes in the northern Chile subduction area (23°S) during the last 330 ky. Quaternary Science Reviews
1045   15(8-9), 819–831. doi:10.1016/S0277-3791(96)00066-2.

1046   Ortlieb, L., Zazo, C., Goy, J.L., Dabrio, C., Macharé, J., 1996b. Pampa del Palo: an anomalous composite marine
1047   terrace on the uprising coast of southern Peru. Journal of South American Earth Sciences 9(5-6), 367–379.
1048   doi:10.1016/S0895-9811(96)00020-X.

1049   Ota, Y., Miyauchi, T., Paskoff, R., Koba, M., 1995. Plio-Quaternary marine terraces and their deformation along the
1050   Altos de Talinay, North-Central Chile. Revista Geológica de Chile 22(1), 89–102.

1051   Paris, P.J., Walsh, J.P., Corbett, D.R., 2016. Where the continent ends. Geophysical Research Letters 43(23),
1052   12,208-12,216. doi:10.1002/2016GL071130.

1053   Pedoja, K., Dumont, J.F., Lamothe, M., Ortlieb, L., Collot, J.-Y., Ghaleb, B., Auclair, M., Alvarez, V., Labrousse,
1054   B., 2006a. Plio-Quaternary uplift of the Manta Peninsula and La Plata Island and the subduction of the Carnegie
1055   Ridge, central coast of Ecuador. Journal of South American Earth Sciences 22(1-2), 1–21.
1056   doi:10.1016/j.jsames.2006.08.003.

1057   Pedoja, K., Husson, L., Regard, V., Cobbold, P.R., Ostanciaux, E., Johnson, M.E., Kershaw, S., Saillard, M.,
1058   Martinod, J., Furgerot, L., Weill, P., Delcaillau, B., 2011. Relative sea-level fall since the last interglacial stage:
1059   Are coasts uplifting worldwide? Earth-Science Reviews 108(1-2), 1–15. doi:10.1016/j.earscirev.2011.05.002.

1060   Pedoja, K., Ortlieb, L., Dumont, J.F., Lamothe, M., Ghaleb, B., Auclair, M., Labrousse, B., 2006b. Quaternary
1061   coastal uplift along the Talara Arc (Ecuador, Northern Peru) from new marine terrace data. Marine Geology
1062   228(1-4), 73–91. doi:10.1016/j.margeo.2006.01.004.

1063   Pilger, R.H., 1981. Plate reconstructions, aseismic ridges, and low-angle subduction beneath the Andes. Geological
1064   Society of America Bulletin 92(7), 448. doi:10.1130/0016-7606(1981)92<448:PRARAL>2.0.CO;2.

1065   Prémaillon, M., Regard, V., Dewez, T.J.B., Auda, Y., 2018. GlobR2C2 (Global Recession Rates of Coastal Cliffs): a
1066   global relational database to investigate coastal rocky cliff erosion rate variations. Earth Surface Dynamics 6(3),
1067   651–668. doi:10.5194/esurf-6-651-2018.

1068   Rabassa, J., Clapperton, C.M., 1990. Quaternary glaciations of the southern Andes. Quaternary Science Reviews
1069   9(2-3), 153–174. doi:10.1016/0277-3791(90)90016-4.

1070   Ramos, V.A., Folguera, A., 2009. Andean flat-slab subduction through time. Geological Society, London, Special
1071   Publications 327(1), 31–54. doi:10.1144/SP327.3.

1072   Regard, V., Saillard, M., Martinod, J., Audin, L., Carretier, S., Pedoja, K., Riquelme, R., Paredes, P., Hérail, G.,
1073   2010. Renewed uplift of the Central Andes Forearc revealed by coastal evolution during the Quaternary. Earth
1074   and Planetary Science Letters 297(1-2), 199–210. doi:10.1016/j.epsl.2010.06.020.

1075   Rehak, K., Bookhagen, B., Strecker, M.R., Echtler, H.P., 2010. The topographic imprint of a transient climate
1076   episode: the western Andean flank between 15.5° and 41.5°S. Earth Surface Processes and Landforms 35(13),
1077   1516–1534. doi:10.1002/esp.1992.

1078   Rodríguez, M.P., Carretier, S., Charrier, R., Saillard, M., Regard, V., Hérail, G., Hall, S., Farber, D., Audin, L.,
1079   2013. Geochronology of pediments and marine terraces in north-central Chile and their implications for
1080   Quaternary uplift in the Western Andes. Geomorphology 180-181, 33–46.
1081   doi:10.1016/j.geomorph.2012.09.003.

1082   Rohling, E.J., Grant, K., Bolshaw, M., Roberts, A.P., Siddall, M., Hemleben, C., Kucera, M., 2009. Antarctic
1083   temperature and global sea level closely coupled over the past five glacial cycles. Nature Geoscience 2(7), 500–
1084   504. doi:10.1038/ngeo557.

1085   Rovere, A., Ryan, D., Murray-Wallace, C., Simms, A., Vacchi, M., Dutton, A., Lorscheid, T., Chutcharavan, P.,
1086   Brill, D., Bartz, M., Jankowski, N., Mueller, D., Cohen, K., Gowan, E., 2020. Descriptions of database fields for
1087   the World Atlas of Last Interglacial Shorelines (WALIS). Zenodo. doi:10.5281/ZENODO.3961544.

1088   Ruh, J.B., Sallarès, V., Ranero, C.R., Gerya, T., 2016. Crustal deformation dynamics and stress evolution during
1089   seamount subduction: High-resolution 3-D numerical modeling. Journal of Geophysical Research: Solid Earth
1090   121(9), 6880–6902. doi:10.1002/2016JB013250.

1091   Saillard, M., 2008. Dynamique du soulèvement côtier Pléistocène des Andes centrales Etude de l'évolution
1092   géomorphologique et datations (10Be) de séquences de terrasses marines (Sud Pérou - Nord Chili), Université
1093   Paul Sabatier, Toulouse.

1094   Saillard, M., Hall, S.R., Audin, L., Farber, D.L., Hérail, G., Martinod, J., Regard, V., Finkel, R.C., Bondoux, F.,
1095   2009. Non-steady long-term uplift rates and Pleistocene marine terrace development along the Andean margin
1096   of Chile (31°S) inferred from 10Be dating. Earth and Planetary Science Letters 277(1-2), 50–63.
1097   doi:10.1016/j.epsl.2008.09.039.

1098   Saillard, M., Hall, S.R., Audin, L., Farber, D.L., Regard, V., Hérail, G., 2011. Andean coastal uplift and active
1099   tectonics in southern Peru: 10Be surface exposure dating of differentially uplifted marine terrace sequences (San
1100   Juan de Marcona, ~15.4°S). Geomorphology 128(3-4), 178–190. doi:10.1016/j.geomorph.2011.01.004.

1101   Santibáñez, I., Cembrano, J., García-Pérez, T., Costa, C., Yáñez, G., Marquardt, C., Arancibia, G., González, G.,
1102   2019. Crustal faults in the Chilean Andes: geological constraints and seismic potential. Andean Geology 46(1),
1103   32. doi:10.5027/andgeoV46n1-3067.

1104   Scholl, D.W., Huene, R. von, 2007. Crustal recycling at modern subduction zones applied to the past—Issues of
1105   growth and preservation of continental basement crust, mantle geochemistry, and supercontinent reconstruction.
1106   In: 4-D Framework of Continental Crust. Geological Society of America, pp. 9–32.

1107   Schwanghart, W., Kuhn, N.J., 2010. TopoToolbox: A set of Matlab functions for topographic analysis.
1108   Environmental Modelling & Software 25(6), 770–781. doi:10.1016/j.envsoft.2009.12.002.

1109   Schweller, W.J., Kulm, L.D., Prince, R.A., 1981. Tectonics, structure, and sedimentary framework of the Peru-Chile
1110   Trench. Geological Society of America Memoir 154, 323–350. doi:10.1130/MEM154-p323.

1111   Shackleton, N.J., Sánchez-Goñi, M.F., Pailler, D., Lancelot, Y., 2003. Marine Isotope Substage 5e and the Eemian
1112   Interglacial. Global and Planetary Change 36(3), 151–155. doi:10.1016/S0921-8181(02)00181-9.

1113   Shepherd, A., Wingham, D., 2007. Recent sea-level contributions of the Antarctic and Greenland ice sheets. Science
1114   (New York, N.Y.) 315(5818), 1529–1532. doi:10.1126/science.1136776.

1115   Siddall, M., Chappell, J., Potter, E.-K., 2006. Eustatic sea level during past interglacials. In: Sirocko, F., Litt, T.,
1116   Claussen, M., Sanchez-Goni, M.-F. (Eds.), The climate of past interglacials. Elsevier, Amsterdam, pp. 75–92.

1117   Simms, A.R., Rouby, H., Lambeck, K., 2016. Marine terraces and rates of vertical tectonic motion: The importance
1118   of glacio-isostatic adjustment along the Pacific coast of central North America. Geological Society of America
1119   Bulletin, B31299.1. doi:10.1130/B31299.1.

1120   Sobolev, S.V., Babeyko, A.Y., 2005. What drives orogeny in the Andes? Geology 33(8), 617–620.

1121   doi:10.1130/G21557AR.1.

1122   Stern, C.R., 1991. Role of subduction erosion in the generation of Andean magmas. Geology 19(1), 78.

1123   doi:10.1130/0091-7613(1991)019<0078:ROSEIT>2.3.CO;2.

1124   Stewart, I.S., Sauber, J., Rose, J., 2000. Glacio-seismotectonics: ice sheets, crustal deformation and seismicity.

1125   Quaternary Science Reviews 19(14-15), 1367–1389. doi:10.1016/S0277-3791(00)00094-9.

1126   Stirling, C.H., Esat, T.M., Lambeck, K., McCulloch, M.T., 1998. Timing and duration of the Last Interglacial:

1127   evidence for a restricted interval of widespread coral reef growth. Earth and Planetary Science Letters 160(3-4),

1128   745–762. doi:10.1016/S0012-821X(98)00125-3.

1129   Strecker, M.R., Alonso, R.N., Bookhagen, B., Carrapa, B., Hilley, G.E., Sobel, E.R., Trauth, M.H., 2007. Tectonics

1130   and Climate of the Southern Central Andes. Annual Review of Earth and Planetary Sciences 35(1), 747–787.

1131   doi:10.1146/annurev.earth.35.031306.140158.

1132   Suárez, G., Molnar, P., Burchfiel, B.C., 1983. Seismicity, fault plane solutions, depth of faulting, and active

1133   tectonics of the Andes of Peru, Ecuador, and southern Colombia. Journal of Geophysical Research 88(B12),

1134   10403–10428. doi:10.1029/JB088iB12p10403.

1135   Taylor, F.W., Frohlich, C., Lecolle, J., Strecker, M., 1987. Analysis of partially emerged corals and reef terraces in

1136   the central Vanuatu Arc: Comparison of contemporary coseismic and nonseismic with quaternary vertical

1137   movements. Journal of Geophysical Research 92(B6), 4905. doi:10.1029/JB092iB06p04905.

1138   Trenhaile, A.S., 2002. Modeling the development of marine terraces on tectonically mobile rock coasts. Marine

1139   Geology 185(3-4), 341–361. doi:10.1016/S0025-3227(02)00187-1.

1140   Turcotte, D.L., Schubert, G., 1982. Geodynamics: Applications of Continuum Physics to Geological Problema. John

1141   Wiley, New York (450 pp.).

1142   Veloza, G., Styron, R., Taylor, M., Mora, A., 2012. Open-source archive of active faults for northwest South

1143   America. GSA Today 22(10), 4–10. doi:10.1130/GSAT-G156A.1.

1144   Venzke, E., 2013. Volcanoes of the World, v. 4.3.4. Global Volcanism Program.

1145   Victor, P., Sobiesiak, M., Glodny, J., Nielsen, S.N., Oncken, O., 2011. Long-term persistence of subduction

1146   earthquake segment boundaries: Evidence from Mejillones Peninsula, northern Chile. Journal of Geophysical

1147   Research 116(B2), 93. doi:10.1029/2010JB007771.

1148   Villegas-Lanza, J.C., Chlieh, M., Cavalié, O., Tavera, H., Baby, P., Chire-Chira, J., Nocquet, J.-M., 2016. Active

1149   tectonics of Peru: Heterogeneous interseismic coupling along the Nazca megathrust, rigid motion of the

1150   Peruvian Sliver, and Subandean shortening accommodation. Journal of Geophysical Research: Solid Earth

1151   121(10), 7371–7394. doi:10.1002/2016JB013080.

1152 von Huene, R., Corvalán, J., Flueh, E.R., Hinz, K., Korstgard, J., Ranero, C.R., Weinrebe, W., 1997. Tectonic
1153   control of the subducting Juan Fernández Ridge on the Andean margin near Valparaiso, Chile. Tectonics 16(3),
1154   474–488. doi:10.1029/96TC03703.

1155 von Huene, R., Scholl, D.W., 1991. Observations at convergent margins concerning sediment subduction,
1156   subduction erosion, and the growth of continental crust. Geology 29(3), 279. doi:10.1029/91RG00969.

1157 Wang, K., Bilek, S.L., 2011. Do subducting seamounts generate or stop large earthquakes? Geology 39(9), 819–822.
1158   doi:10.1130/G31856.1.

1159 Wang, K., Bilek, S.L., 2014. Invited review paper: Fault creep caused by subduction of rough seafloor relief.
1160   Tectonophysics 610, 1–24. doi:10.1016/j.tecto.2013.11.024.

1161 Watts, A.B., Daly, S.F., 1981. Long Wavelength Gravity and Topography Anomalies. Annual Review of Earth and
1162   Planetary Sciences 9, 415–448.